Comparisons of Global Cloud Ice from MLS, CloudSat, and Correlative Data Sets

D. L. Wu[1], R. T. Austin[2], M. Deng[3], S. L. Durden[1], A. J. Heymsfield[4], J.-L. Li[1], G. M. McFarquhar[5], J. V. Pittman[6], G. L. Stephens[2], S. Tanelli[1], D. G. Vane[1], and D. E. Waliser[1]

1. Jet Propulsion Laboratory, California Institute of Technology, Pasadena, California, USA
2. Department of Atmospheric Science, Colorado State University, Fort Collins, Colorado, USA
3. Department of Atmospheric Science, University of Wyoming, Laramie, Wyoming, USA
4. National Center for Atmospheric Research, Boulder, Colorado, USA
5. Department of Atmospheric Sciences, University of Illinois at Urbana-Champaign, Urbana, Illinois, USA
6. NASA Marshall Space Flight Center, Huntsville, Alabama, USA

Date: Jan 20, 2008

Submitted to: *Journal of Geophysical Research -Atmosphere (CloudSat special section)*

Abstract

Aura MLS (Microwave Limb Sounder) V2.2 (version 2.2) and CloudSat R04 (release 4, algorithm version 5.1) ice water content (IWC) and ice water path (IWP) measurements are analyzed and compared to other correlative data. The MLS retrieves IWC at 215-68 hPa with precision (varying between 0.06 and 1 mg/m^3) decreasing with pressure. The IWP products are derived from V2.2 diagnostic cloud-induced radiance (T_{cir}), which are evaluated at the window channels near 115, 240 and 640 GHz. These IWP retrievals correspond to a partial column above 8, 6, and 11 km, with precision of 5, 1.5 and 0.8 g/m^2, and saturate around 2000, 500, and 100 g/m^2, respectively at these frequencies. Our analysis of CloudSat reflectivity shows that the single measurement precision is -31 dBZ, 3 dBZ better than the design specification. Different CloudSat IWC retrievals are generally consistent for IWC < 1000 mg/m^3, but may differ considerably at larger values. The estimated precision for CloudSat IWC varies with height from 0.4 mg/m^3 at 8 km to 1.6 mg/m^3 at 12 km; and the precision for IWP is approximately 9 g/m^2.

MLS and CloudSat cloud ice measurements are compared extensively with correlative data sets for monthly maps and for the normalized probability density function (PDF). To ensure fair comparisons with MLS, CloudSat and other high-resolution data are averaged spatially to match the MLS measurement volume. The resulting MLS and CloudSat IWC maps exhibit similar monthly morphology, and their PDFs agree well with relative difference <50% in the overlapped sensitivity range. However, CloudSat R04 IWC show a significant high biases against MLS at 14-17 km where MLS technique is not limited by sensitivity saturation, and these biases appear to increase with IWC. The maps of MLS partial IWPs show an overall consistent morphology with CloudSat data but it is evident that MLS 115 GHz data lack sensitivity to cloud ice mid and high latitudes. The PDFs of MLS and CloudSat IWP exhibit a consistent slope with bias

generally < 50% in the overlapped sensitivity range. Compared to CloudSat IWP, both MODIS (Moderate Resolution Imaging Spectroradiometer) and AMSU-B (Advanced Microwave Sounding Unit-B) retrievals show a large (~5× and ~8×, respectively) high bias for IWP between 10 and 500 g/m^2. Above 500 g/m^2, both MODIS and AMSU-B sensitivities begin to decay substantially. MLS and CloudSat IWC are also compared to ECMWF (European Center for Medium range Weather Forecasting) and GEOS-5.1 (Goddard Earth Observing System Model, Version 5.1) analyses. We found that the monthly mean ECMWF IWCs are much smaller (by respectively 5× and 20×) than MLS and CloudSat means in cloud ice. Both ECMWF and GEOS-5.1 IWC PDF show a high bias at small IWCs and a low bias for large IWCs against the observations, which cause an overall low bias in average. The precipitation ice is not included in the ECMWF and GEOS-5.1 IWC but should be accounted for a fair comparison with the observations. Reducing retrieval uncertainty due to particle size distribution and a better understanding of cloud vs precipitation ice in the atmosphere are needed in the future studies.

Outline

1 Introduction

Clouds are the major source of uncertainty in understanding and predicting Earth's climate variability and change (Houghton et al., 2001; Randall et al., 2007). The amount of cloud ice in the troposphere, which is critical for atmospheric radiation/energy balance, differs by several folds among the best climate models (Li et al., 2006). This leads to large uncertainties in determining atmospheric radiation, circulation, and other variables or processes. For example, a 1 mg/m^3 error in cloud ice water content (IWC) is equivalent to 10 ppmv error in upper-tropospheric water vapor, which can produce significant greenhouse effects in the atmosphere. Water interchanges between its gas and condensed phases play an important role in determining clouds' response to a perturbed climate, and these height-dependent processes must be understood and quantified adequately as a part of Earth's climate system.

Difficulties of measuring cloud ice with remote sensing arise from cloud variability and microphysics, which are so substantial and complicated that no single instrument, single technique, or single platform can measure them all (Stephens and Kummerow, 2007). One of the major difficulties is the inability of satellite sensors to penetrate some of thick-and-dense clouds. For example, nadir infrared, visible, and UV techniques have difficulty to penetrate far into these clouds to provide ice or water content. Even for the clouds in the scene, some have difficulty to register cloud top height to a correct altitude due to uncertainties in atmospheric temperature profile. For those clouds penetrated by the sensors, knowledge on cloud microphysics, such as particle size distribution (PSD), become a major source of uncertainty, which is needed to infer IWC or ice water path (IWP).

Passive mm and submm-wave techniques have great potential to measure IWC and IWP with abilities of penetrating clouds and interacting with ice scattering along the path (Evans et al.,

1998; Weng and Grody, 2000; Hong et al., 2005; Wu et al., 2005; Eriksson et al., 2007). Measurements from high-frequency instruments like AMSU-B (Advanced Microwave Sounding Unit-B) can provide global coverage of cloud IWP with a broad swath (Zhao and Weng, 2002), as well as a few additional slices of partial IWP column (Hong et al., 2005). The Aura MLS (Microwave Limb Sounder) instrument is one of the latest instruments that apply high-frequency microwave radiometry for cloud ice observations (Waters et al., 2006; Wu et al., 2006). Although it is not designed for swath coverage, it can provide a slightly better vertical resolution than nadir sounders with limb technique by slicing cloud ice layers from the top of the troposphere. The Aura MLS consists of seven radiometers at frequencies near 118, 190, 240, 640 GHz, and 2.5 THz, and is flying in formation with Cloud Profiling Radar (CPR) of CloudSat (Stephens et al. 2002) as part of the NASA A-Train constellation. The synergy of passive-active spaceborne sensors makes a leap forward in cloud remote sensing, from which a large ensemble of multi-frequency observations can help to reduce uncertainties of cloud ice measurements. For example, simultaneous forward and backward scattering signals from ice clouds can be utilized collectively to constrain the microphysical assumptions made in cloud ice retrievals. At present, uncertainties in these assumptions severely affect accuracy of the derived cloud ice measurements. During the normal operation, the Aura MLS (since August 2004) and CloudSat (since June 2006) are currently providing global twice-daily observations from a sun-synchronous orbit. Together with other A-Train instruments such as Cloud-Aerosol Lidar and Infrared Pathfinder Satellite Observation (CALIPSO), Atmosphere Infrared Sounder (AIRS), and Moderate Resolution Imaging Spectroradiometer (MODIS), they offer unique cloud sensitivities from microwave spectra and produce profiles of cloud ice that contribute importantly to the hydrological and radiative budgets of Earth's climate system.

This paper presents a comparative study of cloud ice (IWC and IWP) morphologies and statistics as observed by MLS and CloudSat. The aim of this study is to quantify, in a global sense, the differences among MLS, CloudSat, and correlative data, including MODIS, ARM TWP (Atmospheric Radiation Measurement Program Tropical West Pacific) and AMSU-B (Advanced Microwave Sounding Unit-B). In addition, we also compare the MLS and CloudSat observations with data from global analyses including ECMWF (European Center for Medium range Weather Forecasting) and GEOS-5.1 (Goddard Earth Observing System Model, Version 5.1). By studying them collectively, we hope to gain a better understanding of accuracy, precision, and sensitivity in these data sets and the associated observing techniques.

Because of large spatiotemporal cloud variability and difficulties in obtaining coincident-collocated measurements, we choose to compare IWC and IWP statistics in terms of normalized probability density function (PDF), and use the PDF to characterize properties and differences among various data sets. Because the PDF method requires much less on measurement coincidence and preserve key statistical properties of cloud data (Appendix A), we can use it to characterize measurement noise, bias, and sensitivity collectively from a large ensemble of data, and it is readily for the A-Train sensors to compile a monthly or seasonal ensemble. The paper is organized to describe Aura MLS, correlative, and CloudSat measurements in sections 2-4, followed by the comparative study in sections 5. Conclusions and future work are given in section 6.

2 MLS Data

Aura MLS Experiment

Aura MLS is a passive limb instrument with seven radiometers at frequencies near 118 (H,V), 190(V), 240(H), 640(H) GHz and 2.5 (H,V) THz, of which the 118 GHz and 2.5 THz receivers

measure radiances of both horizontal (H) and vertical (V) polarizations. All the MLS radiometers are sensitive to cloud-induced radiance changes at tangent heights < ~18 km (Waters et al., 2006; Wu et al., 2006). Except for the 118 GHz, all MLS radiometers are double-sideband receivers, which means that the measured radiance is a sum of radiation from two different frequency sidebands that are usually separated by 10-30 GHz. The Aura MLS views forwards in the satellite flying direction, and its (vertical, cross-track) field-of-view (FOV) widths are (5.8, 12), (4.2, 8.4), (3.2, 6.4), (1.4, 2.9), and (2.1, 2.1) km for 118, 190, 240, 640 GHz and 2.5 THz, respectively.

The Aura satellite was launched in July 2004 to a sun-synchronous (~1:40 p.m. ascending crossing time) orbit at 705 km altitude with 98° inclination. The MLS daily coverage ranges between 82°S and 82°N in latitude, and has limb scans synchronized to the orbital period to produce 240 limb scans per orbit during the normal operation. Unlike step-and-stare scans in UARS MLS, Aura MLS scans continuously in tangent height (h_t) from the surface to ~92 km within 24.7s (Waters et al., 2006). The data integration time for each limb measurement is 1/6 second. For GHz measurements, each scan profile has 40-50 limb measurements dedicated to the troposphere with a 300 m sampling resolution in tangent height (Jarnot et al., 2006). These low-h_t measurements are particularly useful for cloud observations.

MLS Cloud Ice Retrievals

The MLS cloud ice is retrieved from T_{cir} of each radiometer at a window channel. The background radiance of the window channels is typically ~20 K for 240 GHz at 100 hPa tangent pressure with precision of < 0.5 K. T_{cir} is defined as the difference between the measured radiance and a modeled background for clear sky. T_{cir} uncertainty is dominated by error of the modeled clear-sky radiance. At high tangent heights where the clear-sky background is relatively

low (< ~100 K), T_{cir} is positive because the radiance from cloud scattering and emission is usually higher than the background. At low tangent heights where the clear-sky background is ~250 K, T_{cir} is negative because the radiance from cloud scattering is lower than the background and blocks the upwelling radiances. Clouds lack contrast from the clear-sky background at the intermediate tangent heights, which makes them difficult to be detected.

The description of MLS cloud-sky forward model and IWC retrieval can be found in Wu et al. (2006) and Wu et al. (2008), respectively. MLS Version 2.2 (V2.2) IWC is retrieved from the 240 GHz T_{cir} measurements at 215-83 hPa, using modeled T_{cir} -IWC relations for conversion. The V2.2 processing computes the T_{cir} profile as a function of tangent height for each scan and for each MLS radiometer, and stores it in a diagnostic file. Like the IWC retrieval, MLS IWP is also retrieved from modeled T_{cir} -*h*IWP relations, where *h*IWP is an ice water path along the MLS LOS. *h*IWP is a partial column of IWP, and is converted to the nadir IWP through geometric relation. In the IWC and *h*IWP retrievals the modeled T_{cir}–IWC or T_{cir}-*h*IWP relations are approximated by a nonlinear function

$$T_{cir} = T_{cir0}(1 - e^{-w/\alpha}) \quad (1)$$

where *w* is either IWC or *h*IWP, and coefficients T_{cir0} and α are given Table 1 and Table 2 for the IWC and *h*IWP, respectively. The T_{cir} –IWC or T_{cir} -*h*IWP relations were modeled by assuming particle size distribution (PSD) (McFarquhar and Heymsfield, 1997) and homogeneously layered clouds for a tropical atmosphere.

MLS V2.2 IWC data were validated in Wu et al. (2008) and compared to CloudSat R03 IWC retrieval for July 2006 and January 2007. MLS IWC measurement should be interpreted as an ensemble average over the large volume near MLS tangent point (see Table 1). The V2.2 IWC

uncertainty is dominated by cloud inhomogeneity and PSD errors. Because the inhomogeneity-induced uncertainties are mostly random, they can be reduced through averaging. However, inhomogeneity-induced scaling error, varying from -70% and +80%, and PSD-induced systematic error (as high as 100-200%) can not be reduced by averaging.

Table 1. Model coefficients for the V2.2 T_{cir} -IWC relations

Ptan (hPa)	Retrieval Coeff. T_{cir0} (K)	α (mg/m^3)	Resolution[a] $H_{\parallel} \times H_{\perp} \times V$ (km^3)	Typical Precision[b] (mg/m^3)
83	100	40	200 × 7 × 5	0.06
100	100	40	200 × 7 × 5	0.07
121	100	43	250 × 7 × 4	0.1
147	90	55	300 × 7 × 4	0.2
177	80	69	300 × 7 × 4	0.3-0.6
215	70	70	300 × 7 × 4	0.6-1.3

a) $H_{\parallel}$, $H_{\perp}$ and V denote, respectively, the along-track, cross-track and vertical extent of the atmospheric volume sampled by an individual MLS measurement.

b) These are typical 1σ precisions of single IWC measurements where the better values are for the extratropics and the poorer values for the tropics.

The standard MLS V2.2 IWP is retrieved from the 240 GHz T_{cir} at a tangent pressure (~650 hPa) near the bottom of each scan. Since the 240-GHz T_{cir} is saturated at 650 hPa due to strong atmospheric attenuation, this limb radiance rarely sees through the atmosphere except for a very dry condition such as wintertime high latitudes. The standard IWP is reported at the tangent point location, but the actual measurement location (where the saturation occurs) is ~300 km (or ~2 nominal MLS profiles) away from the tangent point towards MLS. At 650 hPa the saturated 240-GHz radiance can only penetrate the atmosphere down to ~6 km, which yields a partial column of IWP (pIWP). Hence, the derived 240-GHz IWP is also denoted by $IWP_{>6km}$ to indicate the partial column measured.

In addition to the 240 GHz radiometer, MLS 115, 190 and 640 GHz radiometers can also measure pIWP. As shown in Figure 1, MLS T_{cir} from the four radiometers have different penetration depths, which yield different bottom heights for pIWP. To estimate the bottom height for each MLS radiometer, we compute the transmission function of each window channel, and the associated contribution function by weighting the transmission function with an exponential IWC profile, i.e., $IWC \propto e^{-z/H_0}$, where H_0 is the mean scale height of IWC profiles. Observations from in-situ measurements (Heymsfield and Donner, 1990; McFarquhar and Heymsfield, 1996) suggest that H_0 is ~2 km in the tropical upper troposphere but becomes steeper (~1 km) near the tropopause. We define the bottom of pIWP as the peak altitude of the contribution in Figure 1(b); and they are approximately 8, 7, 6, and 11 km for 115, 190, 240 and 640 GHz. Later in this paper, we also denote these pIWPs as $IWP_{>8km}$, $IWP_{>7km}$, $IWP_{>6km}$, and $IWP_{>11km}$, respectively, for these MLS radiometers.

Table 2 Estimated MLS IWP partial column, precision and sensitivity range

MLS Radiometer	Retrieval Coeff. T_{cir0} (K) | α (kg/m^2)	Bottom Height (km)	Resolution $H_{\parallel} \times H_{\perp}$ (km)	Estimated Precision (g/m^2)
R1 (115 GHz)	-59	19	~8	120 × 12	5
R2 (190 GHz)	-160	9.5	~7	80 × 8	2
R3 (240 GHz)	-180	5.2	~6	60 × 6	1.5
R4 (640 GHz)	-150	1.6	~11	30 × 3	0.8

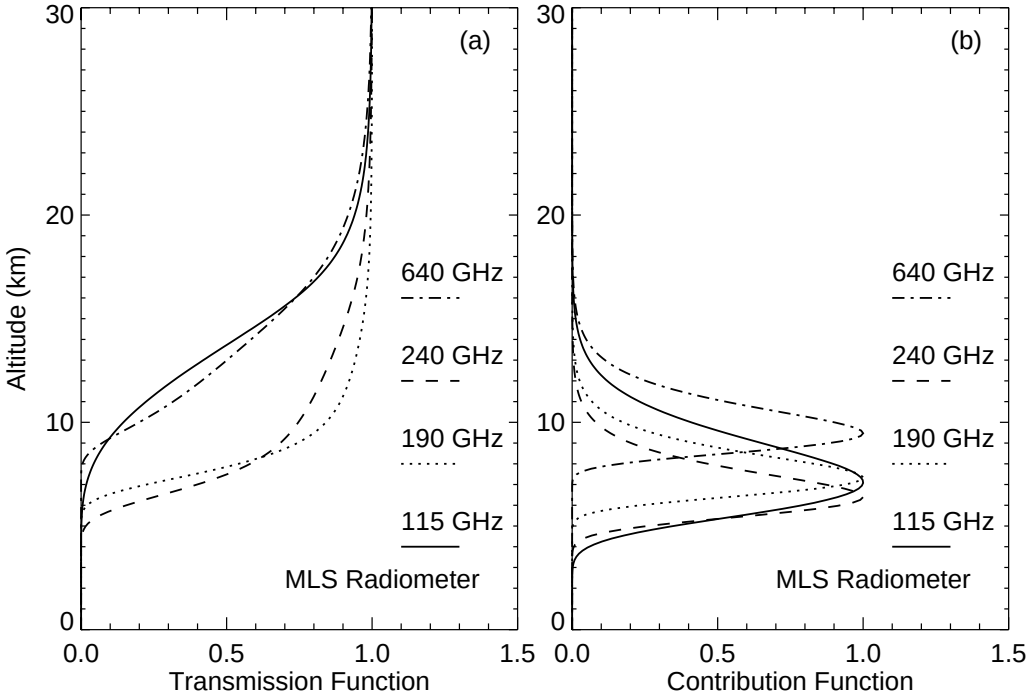

Figure 1 (a) Calculated MLS transmission functions as a function of altitude at the window channel of the 115, 190, 240 and 640 GHz radiometers. (b) Contribution functions to MLS IWP estimated by assuming the IWC vertical distribution in form of $e^{-z/1km}$. The bottom of pIWP is defined as the altitude at which the contribution function peaks, and they are approximately 8, 7, 6, and 11 km for 115, 190, 240 and 640 GHz, respectively.

(c) Spatial Resolution

MLS long limb path has both advantages and disadvantages in sensing upper tropospheric cloud ice. The long path helps to detect cirrus with low ice mass over an extensive area. MLS narrow vertical FOV (3.2 km at 240 GHz) also helps to minimize surface and exclude cloud contributions from altitudes below the pointing tangent height. However, the long limb path smears cloud fields along the LOS, yielding poor horizontal resolution and requiring careful interpretation. Because of the spatial smearing, MLS IWC measurements should be viewed as an ensemble average of clouds (Figure 2). This consideration is particularly important when

comparing MLS cloud ice measurements with other correlative data, and spatial averaging must match to each other for a fair comparison.

Effects of MLS FOV smearing on cloud ice measurements depend on cloud horizontal and vertical inhomogeneity, about which little was known priori to the launch of CloudSat. In the upper troposphere, statistics from in-situ measurements show that the ensemble mean of cloud IWC tends to decrease with height exponentially (McFarquhar and Heymsfield, 1997). This property leads to a simple, nearly-linear relation between MLS T_{cir} and IWC, because the T_{cir}–IWC sensitivity peaks near the pointing tangent height where T_{cir} is measured (Wu et al., 2005). It also serves as the basis of the MLS V2.2 IWC retrieval (Wu et al., 2008). As expected for the coarse horizontal resolution, cloud inhomogeneity may induce error when interpreting an MLS IWC measurement. However, this error appears to be mostly random and can be averaged down in a monthly or seasonal map (Wu et al., 2008). To improve the IWC horizontal resolution, the MLS team is currently developing a tomographic retrieval, which uses information from adjacent scans (separated by ~165 km) to produce IWC profiles at a resolution of ~50 km in distance. Compared to IWC, MLS IWP has a better horizontal resolution (Table 2) because it is measured from a slant viewing angle (Figure 2).

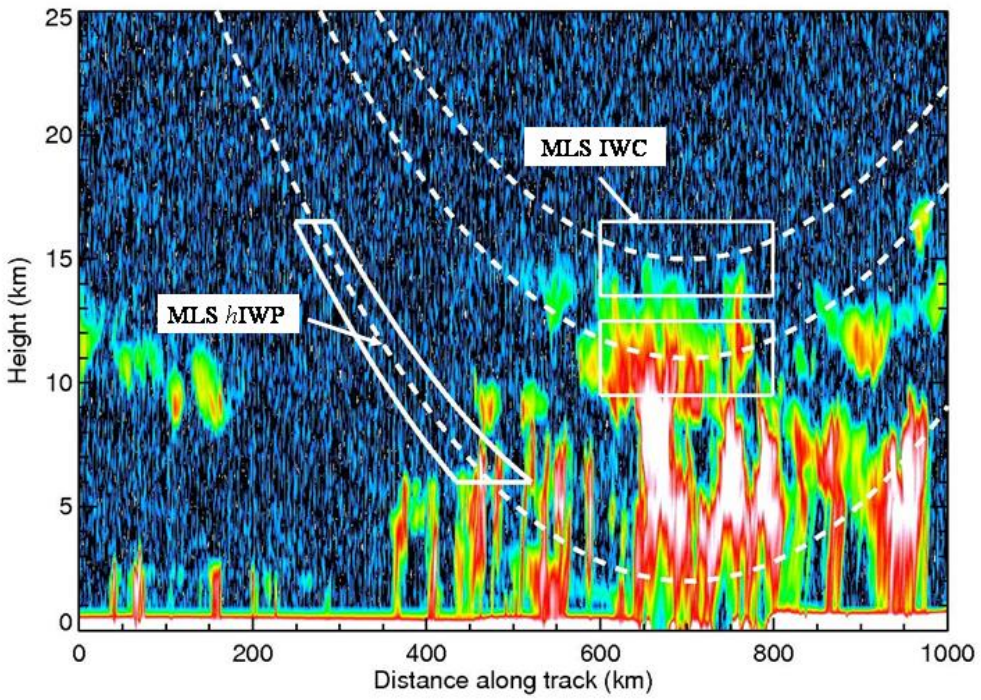

Figure 2. Diagram to illustrate the MLS smearing on the IWC measured by CloudSat. The dashed lines are the MLS tangential beams. At high tangent heights, the beams penetrate through the limb and become sensitive to a volume-averaged IWC, whereas at low tangent heights the MLS beams cannot penetrate through the limb due to strong gaseous absorption and become only sensitive to a partial column of IWP, namely, *h*IWP, with a shallow angle (~3°). Note that the actual volume of the *h*IWP locates at ~300 km away from the tangent point, or ~2 profiles towards MLS.

MLS monthly maps

Cloud ice mass and distribution have profound impacts on global atmospheric circulation and precipitation (Ramanathan et al., 1989; Hartmann and Larson 2002; Stephens, 2005). Research in the past has been focused on effects of clouds on radiation and latent heating at the top or bottom of atmosphere, while the radiative and hydrological processes inside clouds are poorly constrained. The lack of observational constraint on cloud representation in climate models makes the cloud-climate feedbacks problem ill-posed, leading to low confidence on model predictability for future climate changes. The new global observations of cloud ice in the middle and upper troposphere have begun to impose additional constraints on the models, which allow

climate modelers to diagnose and evaluate model physics, parameterization, and predictability in great detail.

Figure 3 and Figure 4 show the monthly maps of MLS 147-hPa IWC and $IWP_{>6km}$ averaged for the period August 2004 - December 2007. Since the MLS V2.2 retro-processing is still in progress, the data processed so far are averaged to give an overview of monthly climatology. The MLS IWC distributions in Figure 3 reflect the transition from an austral-summer season when the main cloud ice features are associated with continental convection over Central Africa and South America, and intense convection over the western Pacific, to a boreal-summer season dominated by the Asian and central American monsoons. These seasonal variations in MLS cloud ice reflect changes of large scale dynamics and variability in regional weather and climate. For example, upper-tropospheric cloud ice from the Asian monsoon occur preferentially in Bay of Bengal and the western Pacific.

In the tropics, MLS IWC distribution correlates well with the intertropical convergence zone (ITCZ). Like in precipitation climatology, the ITCZ features in MLS IWC oscillate with season about the equator but remain at a relatively stationary northern latitude over oceans. However, the IWC distribution in Figure 3 exhibits a large gradient between the eastern and western Pacific, and this gradient varies seasonally with very low cloud ice during December-February. In January-February, cloud ice lifted into the upper troposphere is substantial over the western Pacific warm pool (WPWP) where super convective systems are often formed (Houze et al., 2000). In the meantime (January and February), cloud ice from the southern Pacific convergence zone (SPCZ) also strengthens to its annual maximum. Between May and September, the Asian monsoon brings up spotty and large IWC at latitudes between the equator and 40°N, affecting an area 4-5 times larger than the American monsoon. In October the 147-hPa IWC over the WPWP

region exhibits a distribution pattern very similar to the Gill's solution in response to a large-scale tropical diabatic heating (Gill, 1980), in which an eastward propagating Kelvin wave and a westward propagating Rossby wave are generated. The Kelvin and Rossby wave patterns can be readily seen in weekly MLS IWC maps as well as in MLS RHi (relative humidity with respect to ice) maps. During July-October the $IWP_{>6km}$ enhancement between the eastern Pacific ITCZ and the SPCZ appears to be associated with mid-tropospheric cloud ice since it is not seen in the 147-hPa IWC maps.

The two equatorial bands seen in MLS 147-hPa IWC during March and April over the eastern Pacific are a manifestation of the double ITCZ as reported previously in other satellite observations (Waliser and Gautier, 1993; Lietzke et al., 2001; Halpern and Hung, 2001; Liu and Xie, 2002). The double-ITCZ feature is more pronounced and clearly defined in the IWC maps than in $IWP_{>6km}$. Although it appears in MLS IWC maps at pressure levels between 277 and 121 hPa, the feature is not evident in the 100-hPa IWC map.

Unlike in the IWC maps, the $IWP_{>6km}$ has significant contributions from mid-tropospheric clouds, which is reflected by the cloud ice enhancements at mid and high latitudes (Figure 4). In the Northern Hemisphere, Pacific and Atlantic storms contribute mostly to the mid-tropospheric cloud ice over the oceans during the period between October and January. In the Southern Hemisphere, storms bring up significant mid-tropospheric cloud ice between April and September. In the Tropics, the seasonal variation of $IWP_{>6km}$ is similar to that in the 147-hPa IWC, high in February-October and low in November-January. Note that the Gill's pattern in the October $IWP_{>6km}$ map is not as clear as in the 147-hPa IWC map since the Gill's solution has a characteristic vertical structure that would be smeared out in the integrated cloud ice.

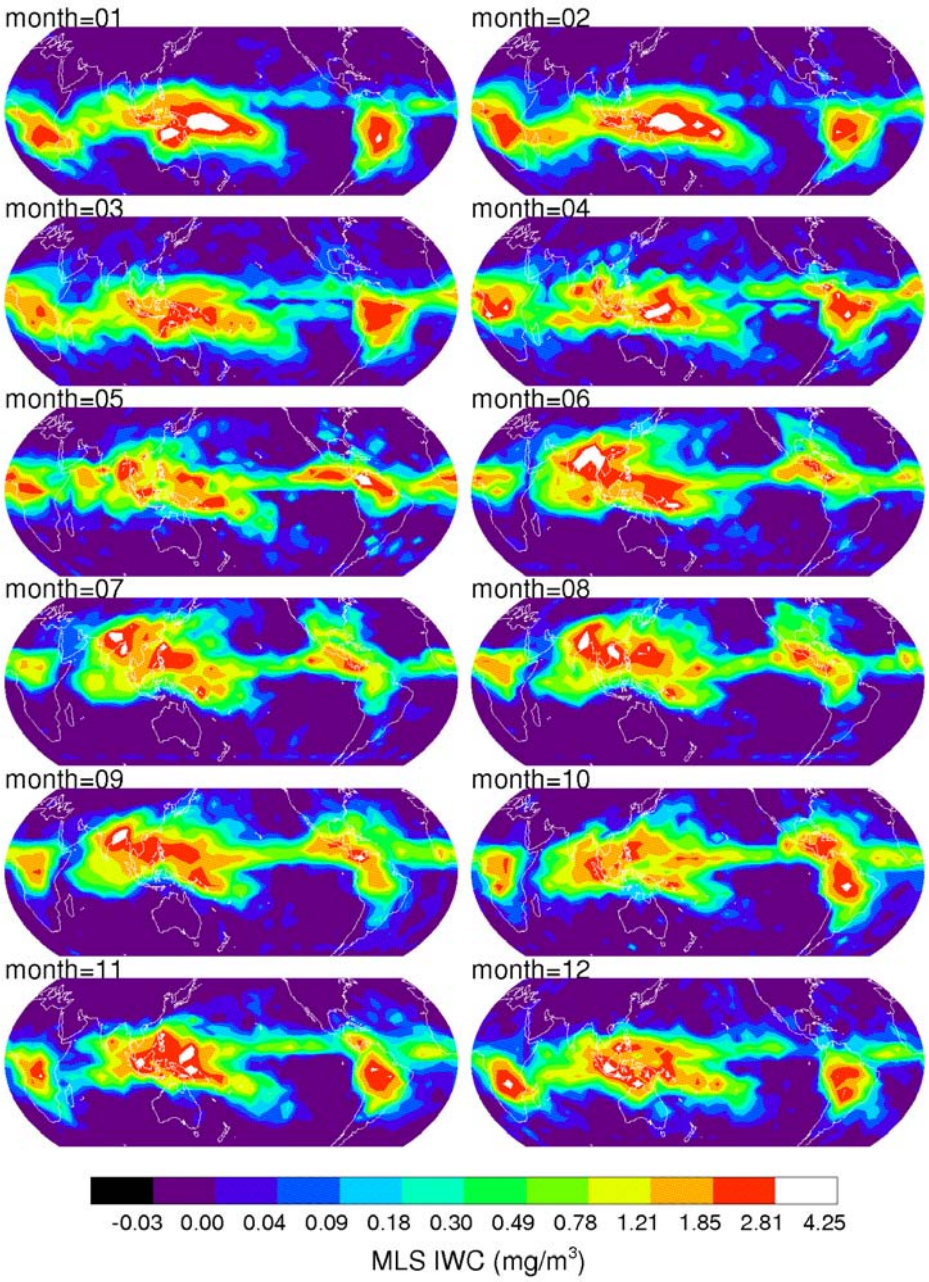

Figure 3 MLS V2.2 monthly mean IWC at 147 hPa for latitudes between 50°S and 50°N from 2004-2007. Both ascending and descending measurements are averaged into 4°×8° latitude-longitude boxes, and the IWC value is an all-sky mean. The IWC data are screened on a daily basis and the values with IWC < 3σ are zeroed.

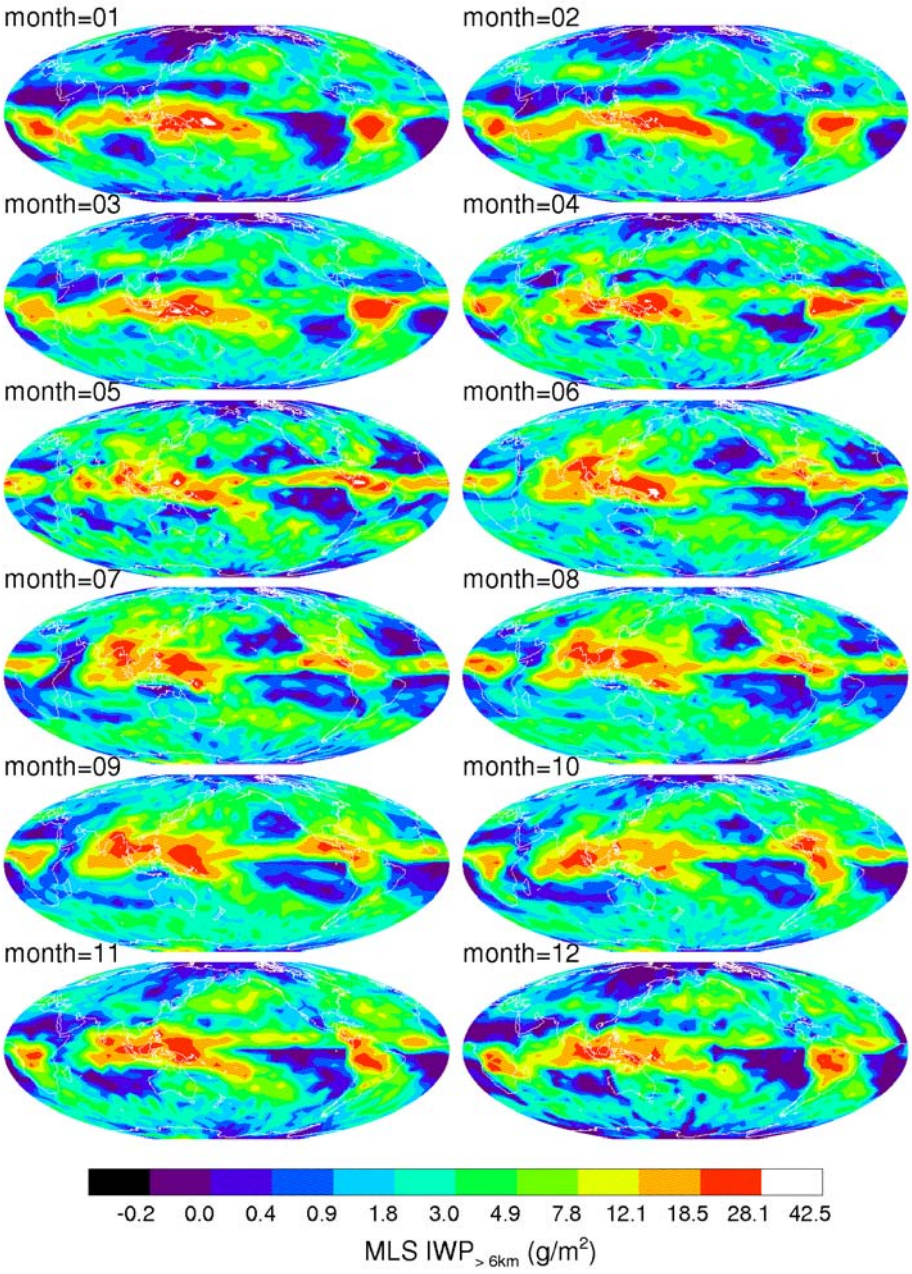

Figure 4 As in Figure 3 but for MLS V2.2 $IWP_{>6km}$ from 2004-2007. The maps are restricted to latitudes between 80°S and 80°N.

3 Correlative Data

CEPEX IWC

Central Equatorial Pacific Experiment (CEPEX) was conducted in the region of 20°S–2°N and 165°E–170°W during March-April 1993 with the campaign focus on cirrus outflows from deep convection. In-situ measurements from CEPEX covered altitudes of ambient temperatures between -70°C and -20°C (Heymsfield and McFarquhar, 1996; McFarquhar and Heymsfield, 1997). CEPEX IWC, mostly observed at ~11.5 km altitude (a cruising altitude) and ranging between 10^{-4} and 1 g/m^3, is derived from measured cloud microphysical properties. At the cruise altitude, the data were collected continuously over a long distance, in which clear and cloudy skies were sampled in a way very much like satellite observations. The data from long-leg flights are particularly useful for comparison to satellite observations because of the fair sampling for clear and cloudy conditions. The another cruise altitude in CEPEX was at ~7 km but with a much shorter duration or coverage than that from 11.5 km.

NAMMA IWC

The NASA African Monsoon Multidisciplinary Analyses (NAMMA) campaign was commenced in August 2006 off the coast of west Africa (10°N-20°N and 10°W-40°W) to study formation and evolution of tropical hurricanes in the eastern and central Atlantic. The IWC data used here are direct measurements from the Counterflow Virtual Impactor (CVI) instrument. The cruise altitude is ~10 km, where more data were collected than other altitudes, but the data were biased toward mesoscale convective systems and sampled often over a short distance. NAMMA flights were designed to probe clouds at different altitudes through spiral sampling, and therefore, cloud statistics from the NAMMA campaign are likely skewed to convective cloud types.

CRYSTAL-FACE IWC

The Cirrus Regional Study of Tropical Anvils and Cirrus Layers-Florida Area Cirrus Experiment (CRYSTAL-FACE or CF) campaign was conducted in July 2002 to study cirrus outflows in the subtropics. The IWC data used in this study were measured by the CVI instrument with uncertainty ranging from 11% at 0.2 g/m^3 to 23% at 0.01 g/m^3. The CVI measurements are saturated at ~ 1 g/m^3. Clouds were sampled mostly from ascending-descending flight paths that cover a height range between -25°C and -52°C. No flights were as long as in the CEPEX campaign with a constant cruising altitude.

ARM Cloud Radar Data

The ARM (Atmospheric Radiation Measurement Program) cloud profiling radars provide long-term ground-based measurements in several sites that contain valuable statistics on cloud ice (Clothiaux et al., 2001; Mace et al. 2001). In this study we use the compiled statistics based on hourly-averaged IWP measurements from the ARM TWP (Tropical West Pacific) sites, namely (0.5°S, 167°E) and Manus (2°S, 147°E) Island, where the IWP is retrieved using the algorithm developed by Deng and Mace (2006). The ARM 35 GHz radar was up for 90% of time at (65% useful) and 44% uptime at Manus in 2005. During the general operation mode, the radar has 90 m range resolution with coherent averaging. Although it is designed to achieve 70 dBZ dynamic range between -50 and +20 dBZ with different operational modes, the estimated minimum cloud sensitivity at and Manus sites is about -41 and -48 dBZ, respectively (Clothiaux et al., 2001).

AMSU-B IWP

The AMSU-B IWP is retrieved with the algorithm developed by Weng and Grody (2000) and Zhao and Weng (2001). The algorithm retrieves IWP and effective diameter D_e simultaneously

retrieved using cloud scattering signatures at 89 and 150 GHz. Thus, the AMSU-B IWP should have a sensitivity similar to MLS 115 GHz, except that the nadir sounder can penetrate slightly deeper in the atmosphere. AMSU-B has better horizontal resolution (15 km at nadir) and swath coverage (2300 km) than MLS. Similar to MLS, the AMSU-B algorithm first estimates the clear-sky radiances at 89 and 150 GHz using the retrieved atmospheric state from AMSU-A 23 and 31 GHz measurements, and then determines T_{cir} from the measured-modeled radiance difference. The derived T_{cir} are not used for IWP retrieval if the value is below a cloud detection threshold, and IWP is zeroed in these cases. The T_{cir}-IWP relation used in the IWP retrieval is modeled by Zhao and Weng (2001), assuming a modified gamma size distribution for ice particles.

MODIS IWP

A MODIS instrument (Salomonson et al., 1989; Barnes et al., 1998) was flown on the Aqua satellite since May 2002, which has the same suborbital track as CloudSat and MLS. It precedes CloudSat by approximately one minute and MLS by ~8 minutes. MODIS measures radiances between 0.4 and 14.2 μm over 36 spectral bands. At nadir, the horizontal resolution ranges from 250 m to 1 km depending on wavelength, and the instrument covers a swath 2330 km wide. In this study, we use Collection 5, daily, daytime, Level 3 data (MYD08_D3) on a 1°×1° (longitude and latitude) gridbox. In this study the MODIS measurements are analyzed at latitudes between 25°N and 25°S for the period between 7 July and 16 August, 2006. IWP is derived from the *ice cloud optical thickness* and the *ice cloud effective radius* products, which are obtained from water-absorbing near-infrared bands (1.6, 2.1, and 3.7 μm) and non-absorbing visible and near-infrared bands (0.65, 0.86, and 1.2 μm), using the following relation (Stephens, 1978):

$$IWP = \frac{4\rho\tau r_e}{3Q_e} \tag{2}$$

where ρ = 0.93 g/cm^3 is the density of ice, τ is the optical thickness, r_e is the cloud effective radius, and $Q_e \sim 2$ is the extinction efficiency. Eq. (2) assumes a vertically uniform effective radius and a constant cloud phase throughout the column, which is determined by the cloud top phase. This calculation and determination is performed with the Level 2 data. The Level 3 data are then reported either as histograms with predetermined IWP bin sizes or as average IWP values within each 1°×1° gridbox. In this study, we do not constrain our analysis to the MODIS predetermined IWP bin sizes. Instead, we use the average IWP value representative of each 1°×1° gridbox. The average IWP approach produces a PDF that is: ~50% higher for IWP less than 10 g/m^2, within ±20% for IWP between 10 and 1000 g/m^2, and 80 to 100% lower for IWP greater than 1000 g/m^2 compared to the histogram IWP approach. The reduction in the frequency of the infrequent and extreme IWP events in the average IWP approach can be explained by the averaging effect on cloud inhomogeneity that takes place within the gridbox. Despite these differences, the use of the average IWP approach in our multi-sensor IWP analysis does not change the conclusions of this study.

ECMWF T_L799L91 Analyses

Most of the modern global analyses can produce a diagnostic product for cloud ice. Despite observation uncertainties and limitations, satellite cloud ice data have demonstrated their values for improving cloud parameterization in global numerical models (Li et al., 2005). Here we make brief comparisons of MLS and CloudSat IWC to the latest data from ECMWF Integrated Forecast System (IFS), T_L799L91 Cycle 30r1, which are output six-hourly at 00, 06, 12 and 18Z for the same period 7 July - 16 August 2006. Cloudy-sky satellite observations are not assimilated in the ECMWF DAS (Chevallier et al. 2004) but microwave information in rainy regions are utilized (Bauer et al. 2002). In other words, cloud properties in the analysis directly

result from the analyzed temperature, humidity and velocity fields according to physics of the cloud scheme. Neither MLS nor CloudSat data are assimilated by the ECMWF DAS.

The $T_L799L91$ model is the latest ECMWF DAS in assimilating atmospheric observations, and has been operational since February 2006. The horizontal resolution of T_L799 gives the highest resolved wavenumber at 50 km, improved from 78 km in T_L511. A better representation of world topography in the new system directly improves forecasts of weather phenomena as well as wave excitation influenced by orographic features. Vertically, the number of model layers is increased to 45-50 levels in the troposphere with a nearly doubled resolution near the tropopause, and 40-45 levels in the stratosphere and mesosphere with the top at ~80 km. Other improvements include a shortened (12 min) time step and an increased horizontal resolution (0.36°) in coupled ocean wave model.

Li *et al.* (2005) compared MLS January IWC observations to an earlier version of ECMWF analysis made on a 1°×1° resolution. A good agreement was found between MLS and ECMWF IWC in the upper troposphere, but MLS is generally higher by a factor of 2-3 over tropical landmasses. A follow-on study extended the analysis for the entire 2005 and took into account the MLS sensitivity limitation (Li et al 2007), which reached a similar conclusion. In studying the model predictability, Li et al. (2007) also found that the model lacks convective activity at pressures > 147 hPa and cannot maintain the initial cloud ice mass at 147 hPa for more than 24 hours, revealing shortcomings in model cloud and convection parameterization schemes.

GEOS-5.1 Analyses

The Version 5.1 Goddard Earth Observing System (GEOS-5.1) data analysis is developed in the NASA GMAO (Global Modeling and Assimilation Office), which has the same physics package as in its earlier version (GEOS-4) (*Bloom et al.*, 2005). GEOS-5.1 adopts the 3D-Var

approach to produce data assimilation every six-hourly (00Z, 06Z, 12Z and 18Z) on 72 model levels from the surface to 0.01 hPa with a 0.5° × 0.67° latitude-longitude resolution. Like the ECMWF analysis, the GEOS-5.1 cloud ice is a diagnostic product, derived from temperature, moisture and other related atmospheric state quantities.

4 CloudSat Data

Launched in April 2006, CloudSat is the first spaceborne 94-GHz cloud profiling radar (CPR) to measure vertical structures of cloud and precipitation (Stephens et al. 2002; Im et al., 2005). Each CPR profile has a range resolution of ~500 m but the measurements are reported on an increment of ~240 m between the surface and ~28 km altitude. The effective dimensions of a single sample are approximately 1.4 km cross-track and 1.8 km along-track with the along-track sampling at every 1.1 km. The 1.8 km along-track resolution results from convolution of the antenna beamwidth (1.4 km) and data integration smearing (1.1 km in distance). Since 16 August 2006, instead of pointing at geodetic nadir, the CloudSat antenna beam was moved to an off-nadir (0.16° in the forward direction) position to reduce specular surface reflectance during the normal operation. In the current A-Train configuration, Aura MLS and CloudSat measurements are separated by 7-8 min in time, but their measurement tracks are separated by ~200 km at low and mid latitudes. Thus, MLS and CloudSat measurements are not collocated for tropical clouds. In early 2008, NASA will move Aura closer to CloudSat and Aqua so that MLS footprints are collocated with CloudSat samples within ±10 km. Under the new A-Train configuration, the MLS and CloudSat observations will allow point-by-point comparative studies for most tropical clouds.

Radar reflectivity factor *Ze* is a fundamental cloud measurement from CPR, which can be derived from the ratio of received (P_r) over transmitted (P_t) power. CloudSat's *Ze* is defined with

respect to liquid water (Li and Durden, 2006). To derive *Ze*, one needs to first evaluate the background noise power (P_n) in P_r, and remove P_n from P_r to deduce the power due to cloud backscattering. Because P_n contains the background emission from the surface and cloud themselves, it is more accurate to estimate P_n on a profile-by-profile basis than relying on measurements from adjacent profiles. An accurate and precise estimate of P_n is critical to determine the minimum detectable cloud reflectivity. In this study we estimate P_n from the P_r measurements at the top 40 bins of each profile (corresponding to altitudes > ~18 km) that are rarely hit by clouds. We exclude contaminated measurements in these 40 bins, which come sometimes from echoes generated beyond the maximum unambiguos range and aliased to the top portion of the 30-km profile window (due to multiple scattering in heavy precipitation cases), and sometimes from rare clouds above 18 km. We remove the contaminations by discriminating spikes that are two standard deviations above/below the estimated mean of the 40 measurements. The retained measurements from 40 are then used to calculate the mean and standard deviation again. Such an estimation procedure is repeated for several (usually < 4) times until the convergence is reached. If all of the 40 measurements are used, the estimated precision for P_n will be improved to $\sigma_n / \sqrt{40}$ or $0.16\sigma_n$, where σ_n is the single measurement precision of CPR at each range bin. The final mean will be the estimated noise power $\hat{P}_n$, and cloud reflected power can be determined by $P_r - \hat{P}_n$. For low signal-to-noise ratio the precision of P_r is dominated by the noise σ_n and the subtraction induces additional noise $\sigma_n / \sqrt{40}$ to σ_n for the resulting cloud reflected power. Hence, the final precision for cloud reflected power is $\sim 1.01\sigma_n$, which is found to be about -31 dBZ in later discussions.

In the officially-released CloudSat data (R04, or release 4, algorithm version 5.1), P_n is calculated with a different method, and CPR reflectivity is set to zero by the 2B-GEOPROF algorithm when it is below P_n (Mace et al., 2007). In the R04 release, IWC is retrieved together with a width parameter that is used to characterize the lognormal size distribution for particle sizes. The radar-only IWC retrieval in R04 (Austin et al., 2008), part of the CloudSat 2B-CWC-RO products, retrieves three particle size distribution parameters as vertical profiles in-situ measurements as the *a priori* constraint. The width parameter and number concentration in an earlier release (R03) is independent of height, which was thought as a primary cause of low IWC biases against MLS at high altitudes (Wu et al, 2008). In both CloudSat R03 and R04 IWC retrievals, IWC is zeroed for cloud temperatures above 0°C and scaled linearly for temperatures from -20°C to 0°C as the partition between ice and liquid water contents. A major improvement with the R04 retrieval is its better handling of intensive cloud cases where the R03 retrieval often failed (Austin et al., 2008). The failed cases are ~2% out of all measurements, which affect significantly the statistics of thick-and-dense clouds. The R04 algorithm is able to retrieve most of these cases and lowers the failure rate to < 0.2%.

In addition to the CloudSat algorithms (Austin and Stephens, 2001; Benedetti et al. 2003; Austin et al., 2008), other methods have been proposed to retrieve IWC from 94-GHz radar reflectivity, most of which use a direct *Ze*-IWC relation derived from ground or airborne observations (e.g., Atlas et al., 1995; Brown et al., 1995; Aydin and Tang, 1997; Liu and Illingworth, 2000; Sassen et al., 2002; Matrosov et al., 2002; Heymsfield et al., 2005; Hogan et al., 2006; Protat et al., 2007; Sayres et al., 2008). These algorithms assume a log-linear relation between *Ze* and IWC, and characterize it with two empirical parameters that are either constant or as a function of temperature and *Ze* (Table 3). We selected two retrievals from the list to

compare with the R04 IWC retrieval: namely, Hogan et al. (2006) (hereinafter H06) and Sayres et al. (2008) (hereinafter S08). However, we modified these *Ze*-IWC relations slightly to include noise propagation by allowing the retrieval of negative *Ze* values. As given Eq. (3), this is achieved by converting the absolute value of *Ze* to IWC using the proposed *Ze*-IWC relation, and assigning the *Ze* sign back to the retrieved IWC, mathematically,

$$IWC = \text{sign}(Ze)a|Ze|^{b} \tag{3}$$

where IWC has unit of g/m^3, and empirical coefficients *a* and *b* can be found in Table 3. Note that radar reflectivity factor *Ze* (mm^6/m^3) in Eq. (3) is taken for its absolute value so that retrieving IWC from negative *Ze* values is enabled. After the conversion, the *Ze* sign is passed to the retrieved IWC. Preserving the full IWC statistics (by including negative retrieval values) is important when comparing averaged CloudSat IWC with other data sets. However, as shown later in Figure 5, the IWC statistics from the 2B-IWC-RO retrieval are truncated.

Table 3. The *Ze*-IWC relations proposed from various studies.

94-GHz *Ze*-IWC Relations	$log_{10}(a)$	*b*	comments[†]
Atlas et al. (1995)	-1.19	0.58	Mid-latitude: FIRE-I
Brown et al. (1995)	-0.82	0.74	Low and mid latitudes: CEPEX (-10°C to -65°C), EUCREX (-10°C to -50°C)
Aydin and Tang (1997)	-0.98	0.48	Model study
Liu and Illingworth (2000)	-0.86	0.64	Low and mid latitudes: CEPEX (-10°C to -65°C), EUCREX (-10°C to -50°C)
Sassen et al., (2002)	-0.92	0.70	Mid and high latitudes: ground Cloud heights: -25°C to -40°C
Heymsfield et al. (2005)			Subtropics: CRYSTAL-FACE Cloud heights: -25°C to -52°C
	-0.17	0.64	$Ze < 0.0032$
	-0.71	0.42	$0.0032 < Ze < 3.97$
	-0.65	0.52	$Ze > 3.97$
Hogan et al. (2006)	-00189*T*-1.19	0.85	Mid-latitude, EUCREX (-10°C to -50°C)
Protat et al. (2007)	-00002*T*-0.61	0.97+0.0046*T*	Low and mid latitudes: CLARE98, CARL99, ARM, EUCREX, FASTEX, CEPEX and CRYSTAL-FACE
Sayres et al. (2007)	-0.89	0.70	Subtropics: CRYSTAL-FACE Cloud heights: 15-17 km

[†] *Ze* is radar reflectivity factor in mm^6/m^3 and *T* is air temperature in °C.

Figure 5 shows the normalized PDFs of CPR reflectivity for $Ze > 0$ and the IWC retrievals from three algorithms (R04, H06, S08). The rising PDF at $Ze < -31$ dBZ in Figure 5(a) is a manifestation of the Gaussian noise from the measurement. The -31 dBZ standard derivation is the best fit to the rising PDF at small positive values as well as negative values (not shown). This estimated CloudSat *Ze* noise is 3 dBZ better than the -28 dBZ design requirement (Im et al., 2005; Tanelli et al., 2008). The PDFs at $Ze > -31$ dBZ are dominated by cloud contributions, showing a log-linear distribution over a broad dynamic range between -31 and 15 dBZ. Cloud occurrence diminishes sharply at $Ze > 20$ dBZ in the upper troposphere although the CPR can measure a reflectivity of 40 dBZ. As an interesting cloud property, the *Ze* PDFs all maintain approximately the same log-linear slope, or PDF $\sim Ze^{-1}$, at altitudes above 12 km where cloud occurrence frequency drops exponentially with height. The *Ze* PDF slope turns shallower, or PDF $\sim Ze^{-0.9}$, at altitudes < 12 km, and reveals moderate saturation at $Ze > 10$ dBZ and severe saturation at $Ze > 15$ dBZ, as expected for Mie scattering effects at 94 GHz.

The IWC retrievals from CloudSat *Ze* can differ considerably from each other depending on the method used. Figure 5(b-d) compare the R04, H06, and S08 IWC retrievals with aircraft measurements from CEPEX, CRYSTAL-FACE and NAMMA campaigns at 8, 10, and 12 km. The PDFs of the three CloudSat IWC retrievals agree well for IWC < ~700 mg/m^3 but show significant differences at high IWC values. Overall, the R04 retrieval is closer to S08 at these altitudes, both biased low against H06. Because of the log-linear *Ze*-IWC relation used by H06 and S08, the *Ze*-to-IWC conversion also distorts the Gaussian distribution. Note that the noise of R04 IWC retrieval produces a flat PDF, due to the noise truncation, for values below its noise. At IWC > 700 mg/m^3, PDF differences among three CloudSat retrievals may be resulted from the microphysical assumptions made by these methods. The high bias with the H06 method, as noted

in H06, could be due to its ice density model, which is inappropriate for the applications involving large ice particles. Heymsfield et al. (2007) also compared radar IWCs retrieved from various methods, and found that the H06 method would produce a high bias at large IWCs for temperatures between -20°C and -50°C but the bias is smaller at temperatures < -60°C. Eriksson et al. (2008) also evaluated CloudSat R04 and R03 retrievals and compared them to those from Liu and Illingworth (2000) and from a method using the MH97 size distribution. They found that the retrieval from Liu and Illingworth (2000) agrees well with one from the MH97 method, both having a PDF between those from the R03 and R04 retrievals.

To validate the PDF slope in the upper troposphere, we compare the PDFs of in-situ IWC measurements with CloudSat IWC in Figure 5(b-d). The PDF slope reflects nature of cloud inhomogeneity and horizontal variability of atmospheric dynamics. Because these cloud campaigns were designed to go after cloudy atmospheres, the observed cloud occurrence frequency may be biased high, compared to the global tropical statistics from CloudSat. Overall, the CloudSat PDF slopes agree reasonably well with CEPEX at 12 km and with the CRYSTAL-FACE statistics at all three altitudes. The PDF slopes of the in-situ data show large differences at 8 and 10 km, likely due to sampling biases by these campaigns.

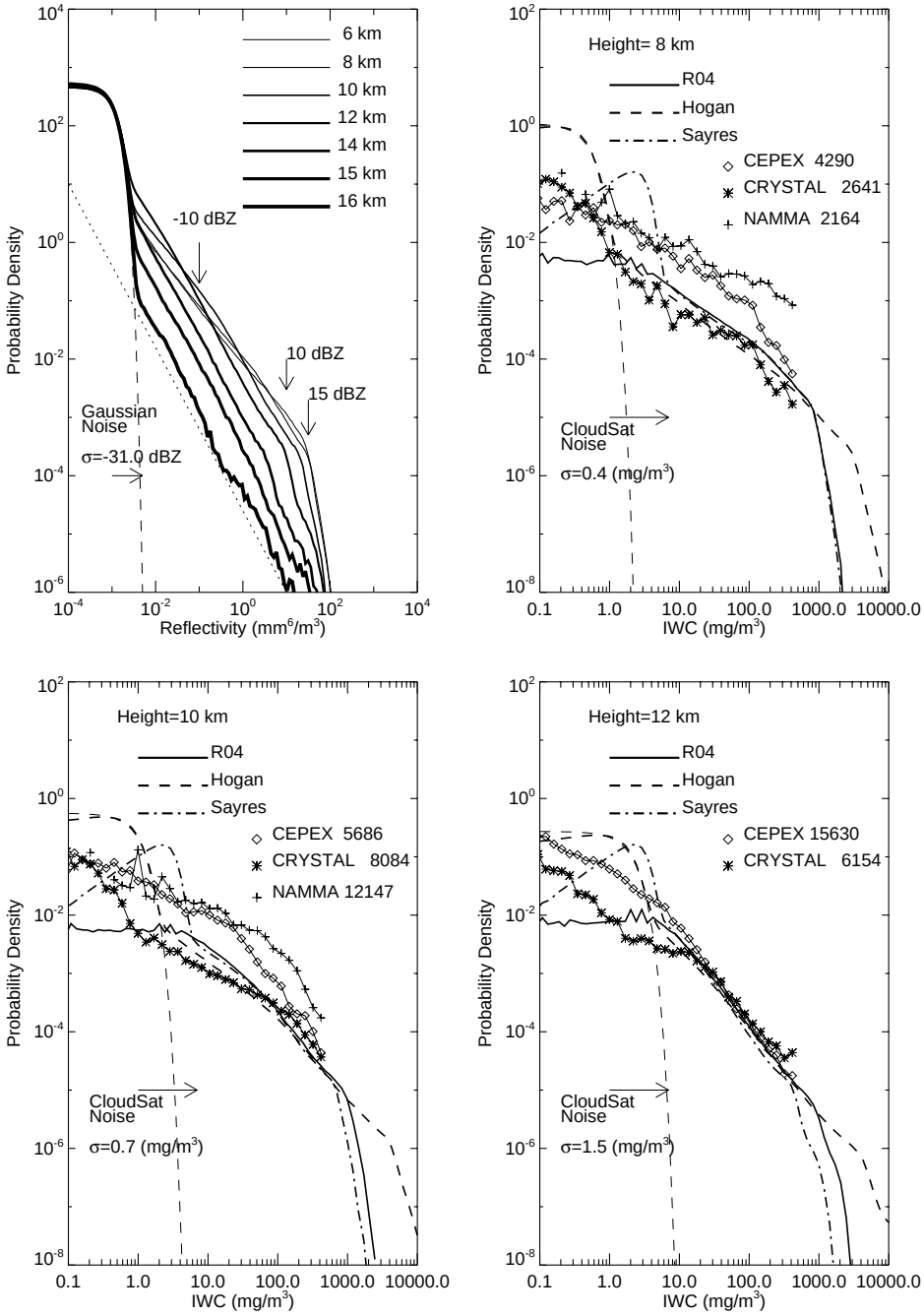

Figure 5. Normalized PDFs of CloudSat (a) reflectivity *Ze* and (b-d) IWC at 8, 10, and 12 km for 7 July-16 August 2006 in a tropical bin (25°S-25°N). The rising PDF at small *Ze* is a manifestation of Gaussian noise with the standard deviation of -31 dBZ. The dotted line indicates the slope of PDF with Ze^{-1}, which appears to be universal at altitudes > 12 km. CloudSat *Ze* PDF drops sharply at *Ze* > 15 dBZ at altitudes ≤ 10 km, indicating strong attenuation by clouds. The PDFs of negative *Ze* values are not shown since they are similar to the rising PDF at small positive values. The CloudSat IWC noise is estimated from the H06 method with the standard deviation shown, whereas the estimated error from the S08 method would be 2-5 times larger depending on altitude. The PDF of the R04 retrieval appears to be white at IWC < ~4 mg/m^3, losing the Gaussian characteristics due to the cloud masking algorithm. The number of in-situ IWC measurements from CEPEX, CRYSTAL-FACE, and NAMMA campaigns are indicated after the acronym.

5 Cloud Ice Comparisons

Spatial Averaging

Comparing cloud ice measurements is challenging because of large cloud inhomogeneity and variability. As a bulk quantity, the IWC and IWP measurements represent an spatial average of cloud ensembles. Because the measurement volume may differ from instrument to instrument, the observed IWC or IWP statistics may be different. As shown in Figure 2, MLS IWC measurements correspond to a tangential volume over ~300×7×4 km^3, whereas a CloudSat measurement has a volume of ~1.8×1.4×0.25 km^3 in the along-track, cross-track and vertical dimensions. Thus, for a fair comparison we need to take in account the averaging effects imposed by each technique. One way to minimize spatial averaging effects is to average the data set with finer spatial resolution to match the measurement volume of lower resolution.

Effects of spatial averaging on cloud ice statistics is difficult to evaluate without knowing the true cloud variability. Before the launch of CloudSat, information on IWC inhomogeneity is very limited. In-situ measurements from aircraft campaigns in the past have very few long-leg flights, and the samplings are biased toward several cloud types (e.g., cirrus and outflow anvils). Convective cores and mesoscale convective systems are often too dangerous to send airplanes. Therefore, instead of evaluating averaging effects on MLS measurements, we compare MLS and CloudSat measurements directly by averaging CloudSat data to match MLS measurement volume.

Cloud vs. Precipitation Ice

Remotely-sensed IWC or IWP are different from the quantity produced by numerical models, and observation-model comparisons must be interpreted with caution in terms of cloud and

precipitation ice. Most of the observing techniques based on ice particle scattering can not distinguish between cloud and precipitation ice. The precipitation ice (i.e., snow flakes, graupels) is often associated with large ice crystals and a substantial falling speed. Scattering effects from cloud and precipitation ice particles are usually mixed together to produce reflectivity in the active case or T_{cir} in the passive case. Therefore, the remotely-sensed IWC is likely a combination of cloud and precipitation ice. On the other hand, cloud and precipitation ice are usually treated differently in the numerical models. What are output by ECMWF and GEOS-5.1 analyses are only for cloud ice, but ice mass associated with snow and precipitation can be derived separately (Waliser et al., 2008).

IWC Comparisons

Figure 6 shows the IWC maps from MLS, ECMWF and CloudSat averaged at pressure altitudes of 10.7, 12, 13.3, 14.7, and 16 km for 7 July-16 August 2006. The IWC morphology is consistent among the three data sets, showing similar enhancements in the Asian and American monsoon regions. CloudSat mean IWC is generally 3-5 times greater than MLS ones, and both observations are greater than the ECMWF mean. Some MLS clouds at Southern Hemispheric high latitudes, showing latitude strips, are artifacts from false detection with the V2.2 algorithm (Wu et al., 2008). The V2.2 cloud detection threshold is generally improved over V1.5 but false detection remains large at high latitudes and affects the IWC average if it is < 0.15 mg/m^3. The enhancement over the southern Argentina at 10.7, 12, and 13.3 km is captured by MLS, CloudSat, and ECMWF but the ECMWF amplitude is much weaker than the observations and CloudSat can even see it at 14.7 and 16 km. In the Northern Hemisphere MLS cloud ice distribution is overall consistent with CloudSat at 10.7-16 km except CloudSat values are biased high, which cause partly the wider (northward) spread of IWC distribution at 13.3-16 km.

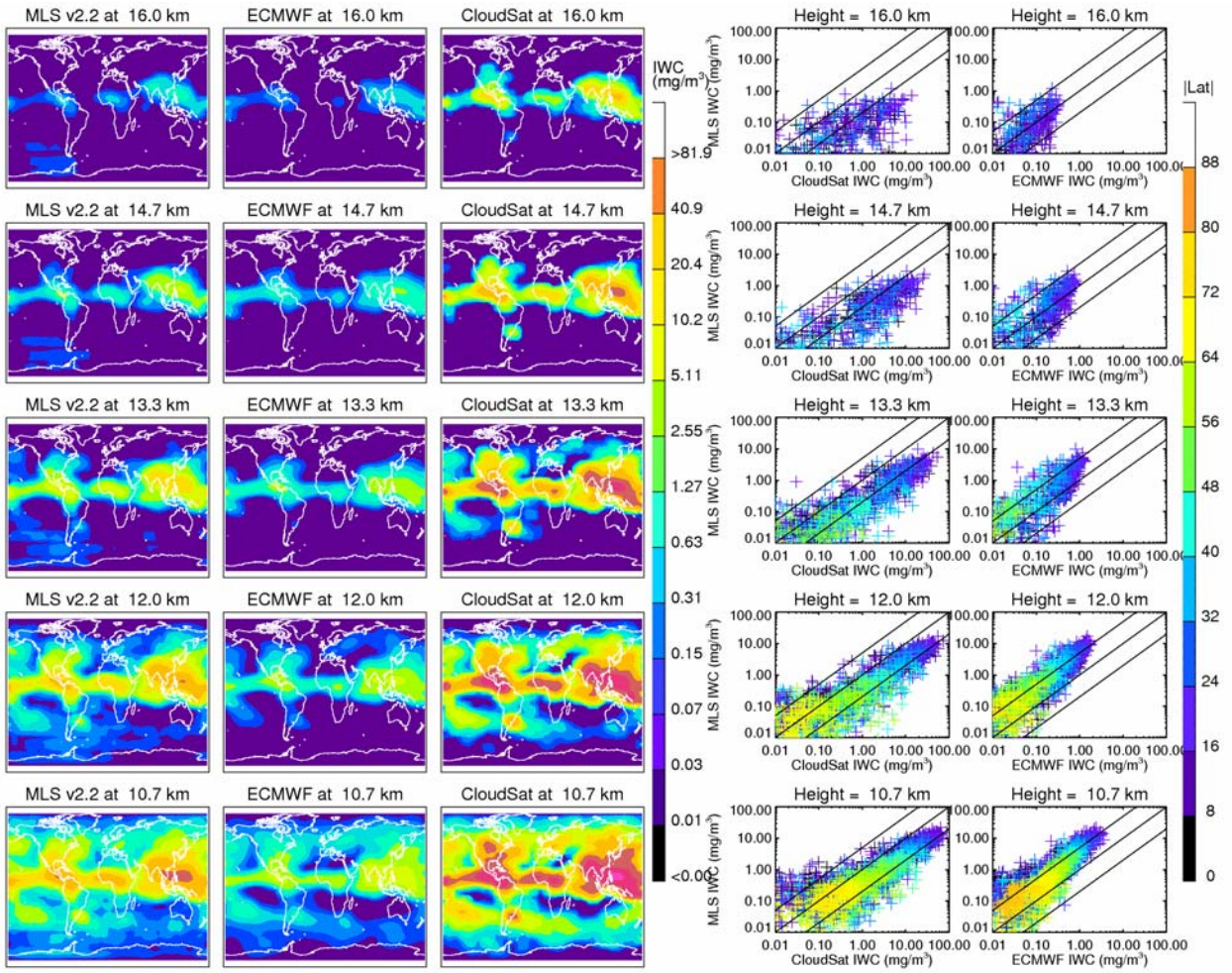

Figure 6. MLS, ECMWF, and CloudSat and IWC maps for 7 July-16 August 2006 at pressure altitudes of 10.7,12, 13.3, 14.7, and 16 km. The maps have the same color scale on a 4°×8° Lat-Lon grid, and a 3-point smoothing is applied to the gridbox averages. The striping distribution in MLS IWC maps at mid-and-high southern latitudes are artifacts of false detection. The ECMWF and CloudSat IWC data are averaged vertically to match the MLS vertical resolution (~4 km) at these altitudes. On the right are scatter plots of the IWC values from the maps, where colors denote latitudes from the equator and lines of the 1:1, 1:5, and 5:1 ratios are shown.

The monthly mean ECMWF IWCs at 10.7-16 km are generally lower compared to MLS and CloudSat by a factor of ~5 and ~20, respectively. ECMWF lacks mid-latitude cloud ice at 10.7-13.3 km altitudes, although the model captures the feature over the southern Argentina. The H06 and S08 IWC retrievals (not shown) have a mean and distribution similar to the R04 retrieval.

As aforementioned, the gridbox average in IWC maps is not the proper evaluation for measurement bias because sensitivity differences are neglected. A better way to characterize the

measurement bias, among other statistical properties, is with the normalized PDF. Figure 7 shows comparisons of the PDFs of MLS, CloudSat and ECMWF IWCs at altitudes of 10.7-17.3 km where the CloudSat and ECMWF IWCs are averaged horizontally and vertically to match the MLS measurement volume (Figure 2). The comparisons in Figure 7 are restricted to the tropical region (25°S-25°N), which contains most of the cloud ice in the upper troposphere. For the H06 and S08 IWC retrievals, the measurement noise of CloudSat IWC averaged the for MLS volume is estimated by fitting the rising PDF at small IWC values with a Gaussian function. Similarly, the ECMWF and GEOS-5.1 IWCs are averaged to match the MLS measurement volume.

The measurement noise, bias, and sensitivity range of MLS, CloudSat, ECMWF and GEOS-5.1 data sets can be summarized with Figure 7. The MLS, H06 and S08 retrievals have a rising PDF at small IWC values, which is dominated by the measurement noise, whereas the R04 retrieval does not because of the truncation by the retrieval. The estimated MLS and CloudSat IWC noises show that at 16 and 17.3 km MLS has a slightly better precision than CloudSat, but worse at lower altitudes. MLS sensitivity also degrades for large IWC values due to saturation by thick-and-dense clouds (Wu et al., 2008). This degradation in MLS sensitivity reflects fewer large IWC measurements, causing a sharp drop in the PDF tail and contributing largely to the low bias against CloudSat. CloudSat sensitivity to IWC, on the other hand, has a wider dynamic range because of better cloud penetration ability with the radar. The three CloudSat IWC retrievals show a consistent IWC PDF up to ~700 mg/m^3 before deviating significantly from each other. As discussed above, the R04 IWC PDF is overall more consistent to S08, but both are lower than H06 at large IWC values.

In the overlapped sensitivity range, the MLS and CloudSat IWC agree reasonably well at these altitudes, showing the PDF differences less than 50%. The MLS-CloudSat differences

exhibit somewhat larger differences at 16 and 17.3 km, where MLS have its best sensitivity, with MLS being lower against CloudSat R04 IWC. The biases appear to increase with IWC in the overlapped sensitivity range. In a comparison to R03 data, the MLS-CloudSat bias was found to be much smaller at these altitudes (Wu et al., 2008). Nonetheless, the agreement between MLS and R04 IWC PDF is very encouraging overall, particularly at altitudes < 14.7 km. At altitudes > 14 km, however, the high bias in CloudSat R04 retrieval warrants further investigation.

The ECMWF IWC, although showing the global distributions similar to MLS and CloudSat in Figure 6, exhibits quite different PDFs in Figure 7. The ECMWF PDFs are generally biased high (by a factor of 5-8) at small (< 5 mg/m^3) IWCs but low at large (> 5 mg/m^3) IWCs. At all altitudes, the ECMWF PDF drops off too sharply at large IWCs but manages to maintain the same slope at small IWCs. In other words, cloud occurrence frequency appears too high for small cloud ice values but too low for large ice values. The sharp dropoff at large IWCs could be resulted from the cloud ice removal/precipitation processes in the model As discussed in the beginning of this section, the ECMWF IWC is only for cloud ice and does not include snow or precipitation contributions.

The GEOS-5.1 IWC, like the ECMWF IWC, has a high bias at small IWCs and a low bias at large IWCs, but it agrees better with the observations at the large IWC end. Nonetheless, the GEOS-5.1 PDF still drops too sharply and lacks large IWC values in statistics. The largest differences between GEOS-5.1 and ECMWF IWCs are in the range of 5-50 mg/m^3 where the GEOS-5.1 PDF tends to drop off more gradually. For the monthly mean IWC (not shown), GEOS-5.1 values are slightly higher than MLS but lower than CloudSat R04 retrievals.

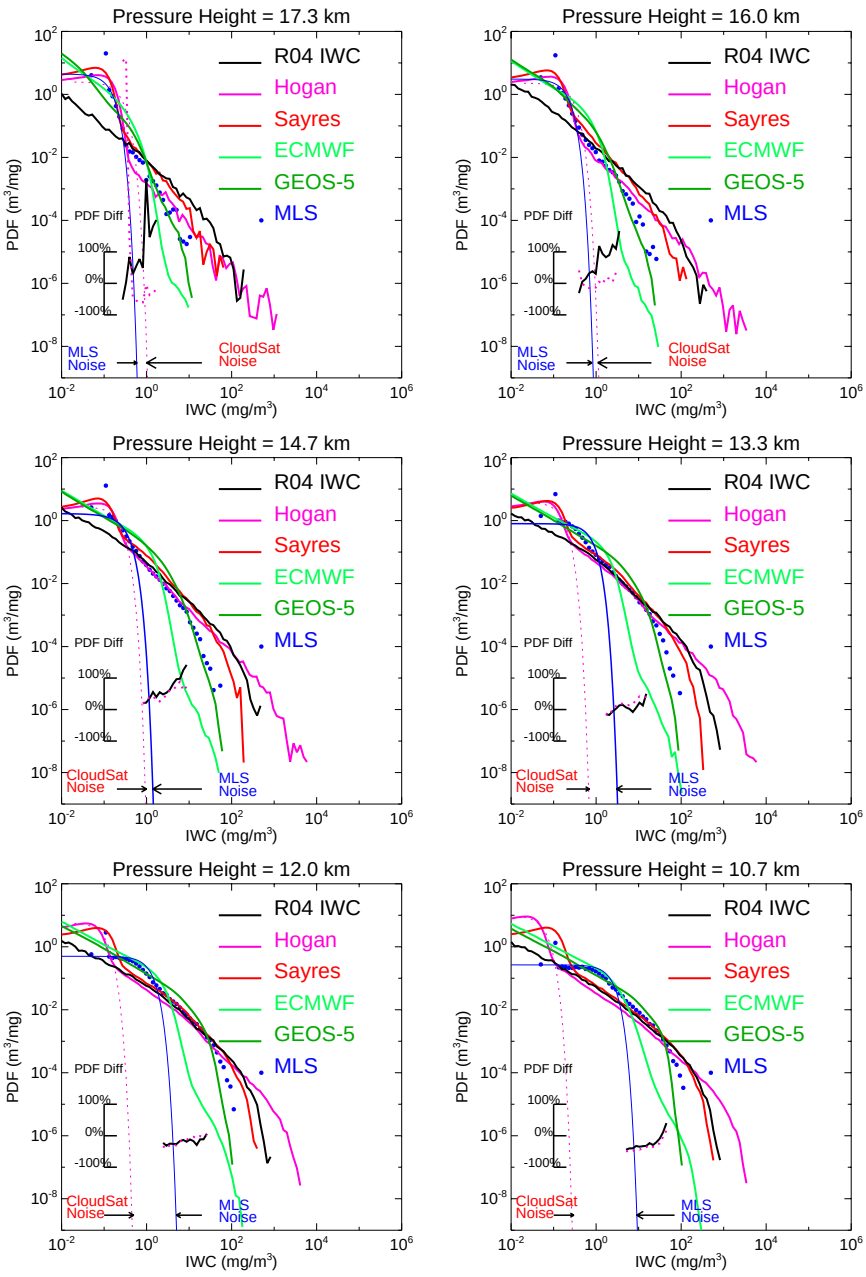

Figure 7. PDFs of ECMWF, GEOS-5, MLS, and CloudSat IWC for 7 July-16 August 2006 in a tropical bin of 25°S-25°N. Seven pressure levels at 261, 215, 177, 147, 121, 100, and 83 hPa, which correspond to nominal altitudes of 10.7, 12, 13.3, 14.7, 16, and 17.3 km, respectively are presented. Three CloudSat retrievals (R04, H06, and S08), are shown to highlight large differences at IWC > ~30 mg/m^3. The IWC retrievals from H06 and S08 start to deviate at IWC > ~100 mg/m^3. Rising PDFs at small IWC values are manifestations of the measurement noise, and the fitted Gaussian curves are shown with the estimated CloudSat (H06) and MLS Gaussian noise indicated. The short curves in the lower part of each panel with scale on the left are the PDF percentage difference between CloudSat (R04 and H06) and MLS IWC. Only the percentage differences in the overlapped sensitivity range are shown, which is defined as (CloudSat-MLS)/CloudSat * 100 and labeled inside each panel.

IWP Comparisons

IWP is more difficult to compare than IWC. Additional uncertainties in the IWP retrieval, such as the column height and contamination of liquid clouds, can all contribute to observed differences. For passive sensors, penetration depth sometimes varies largely with water vapor loading and cloud self-absorption in the atmosphere. The same IWP value may correspond to different column bottoms if the tropospheric water vapor profile is different. In the limb-viewing case, MLS 115, 190, 240, and 640 GHz window channels have a bottom at ~8, ~7, ~6, and ~11 km on average, but the bottom height of individual measurements may deviate somewhat from these estimates. In the cases of precipitating and mixing-phase clouds, absorption/attenuation by liquid clouds in the lower troposphere can further complicate the IWP retrieval and cause reduction of IWP sensitivity because the attenuation from liquid water is much stronger than vapor. IWP measurements tend to have larger uncertainty in mixed-phase cloud cases (e.g., in polar regions), where temperatures are near or warmer than -40°C (Hogan et al., 2003).

Like IWC, an IWP retrieval is also affected by uncertainties in the assumptions made about cloud microphysics, such as particle size distribution and ice density. This error source is frequency-dependent, but IWP column bottom height and sensitivity are likely the dominant sources of retrieval errors. To quantify measurement errors, we first compute pIWP from CloudSat IWC that best match MLS IWP measurements using the estimated MLS column bottom. Then, we compare maps and PDF to assess pIWP error, bias, sensitivity differences from various sensors. Similarly, we compute the pIWP from ECMWF and GEOS-5.1 IWC to compare with correlative observations.

As shown in Figure 8, MLS, CloudSat, and ECMWF IWPs exhibit similar distributions for the three pIWPs defined by MLS penetration depth. However, there are some differences. Lack

of mid and high latitude cloud ice in MLS 115-GHz map is unlikely due to the penetration depth difference because the depths of MLS 115 and 240 GHz pIWP are approximately same and these clouds are evident in the 240-GHz map. The missing mid-latitude clouds may suggest poorer cloud sensitivity with the 115 GHz channel. On the other hand, lack of cloud ice at mid and high latitudes in the 640 GHz map, compared to the 240-GHz map, are likely due to different penetration depths associated with these frequencies. Even though the 640-GHz channel has better sensitivity to cloud scattering than 240 GHz, it cannot penetrate deep enough to see clouds in the lower atmosphere. Compared to the observations, the ECMWF pIWPs are generally lower, which may explain lack of ECMWF cloud ice above 8 km over the northern Africa and the Rockies. Furthermore, the ECMWF $IWP_{>11km}$ misses most of the cloud ice at mid and high latitudes, and the cloud ice over the SPTZ is weak compared to the observations.

The correlation of gridbox pIWP averages from MLS and CloudSat are widely scattered (top panel in Figure 8). In the $IWP_{>8km}$ case, MLS 115 GHz measurements have a slightly high bias for large $IWP_{>8km}$ values but a low bias for small values. The values with a high bias are located mostly at low latitudes. The correlation between MLS 240 GHz and CloudSat $IWP_{>6km}$ falls between the 1:1 and 1:5 lines with MLS being lower. The low MLS bias is also evident in the $IWP_{>11km}$ scatter plot.

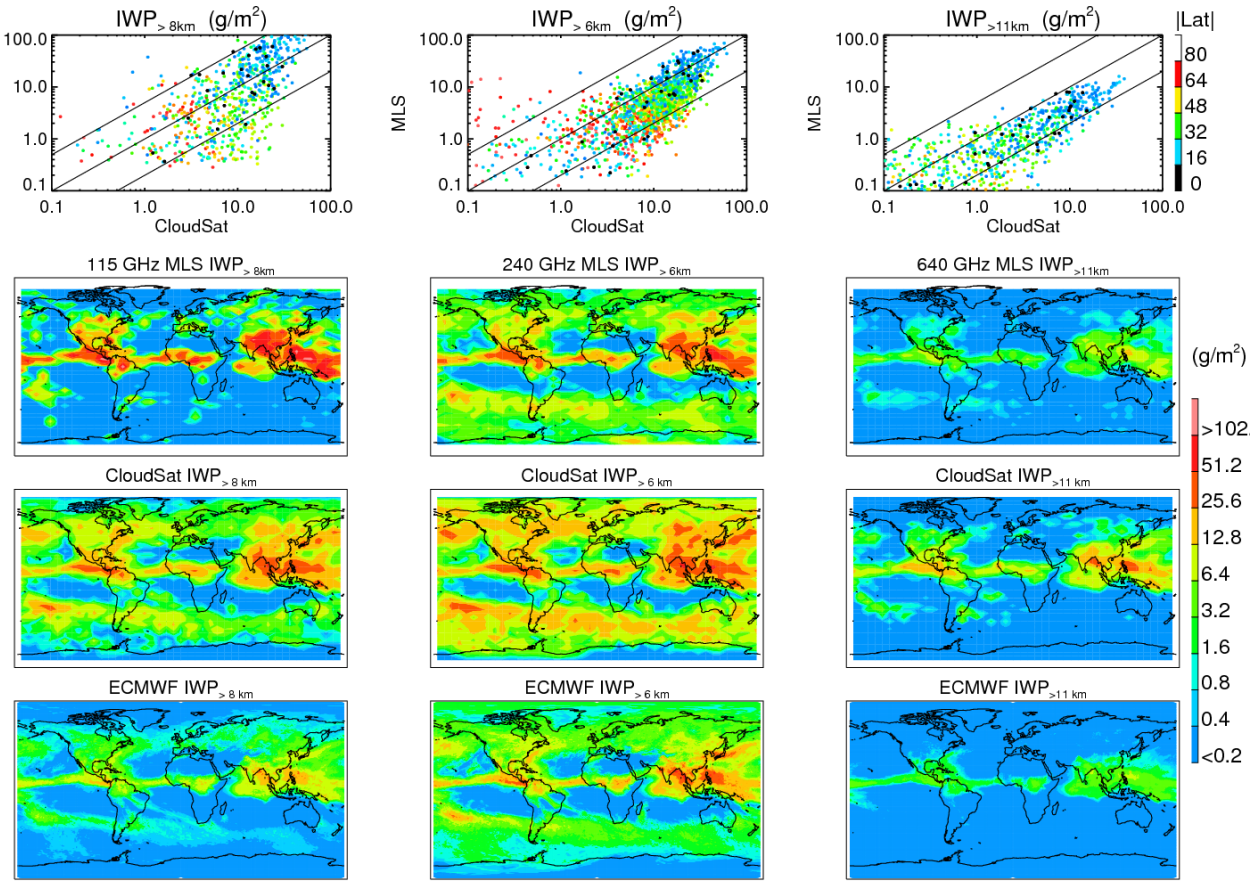

Figure 8. MLS, CloudSat, and ECMWF IWP maps (4° × 8° latitude-longitude grid) for 7 July-16 August 2006. The three partial columns, $IWP_{>8km}$, $IWP_{>6km}$, and $IWP_{>11km}$, are based on MLS 115, 240 and 640 GHz measurements. All IWP maps share the same color scale on the right, and a 3-point smoothing is applied to the averages. Correlation between MLS and CloudSat gridbox averages is shown in the top row with latitude in colors, and the 1:1, 1:5 and 5:1 ratios are shown to guide comparisons.

The scattered relations between MLS and CloudSat pIWPs in Figure 8 are partly due to differences in measurement noise and sensitivity. Figure 9(a-c) compare the PDFs of MLS and CloudSat pIWPs from a tropical (25°S-25°N) bin during the period 7 July-16 August 2006. There is a dip at ~50 g/m^2 in Figure 9a, and MLS $IWP_{>8km}$ is overall lower than CloudSat for values greater than ~50 g/m^2. For all pIWP PDFs in Figure 9a, the H06 and S07 retrievals agree well with each other but drop more sharply than R04 at the large pIWP end. In this case (MLS 115 GHz), there is a broad sensitivity overlap (20-3000 g/m^2) between MLS and CloudSat $IWP_{>8km}$, where MLS agrees generally well with CloudSat R04 and S08 retrievals.

From the PDFs in Figure 9b, we estimate the precisions of MLS 240-GHz and CloudSat $IWP_{>6km}$ retrievals, and they are comparable (1.1 and 1.5 g/m^2, respectively). Both retrievals agree well in the overlapped sensitivity range (5-300 g/m^2). The sharp dropoff in the MLS PDF at pIWP > 300 g/m^2 suggests saturation in MLS sensitivity. In the saturation cases MLS can still detect clouds but may underestimate the pIWP value. The CloudSat R04 and S08 retrievals in the $IWP_{>6km}$ case agree well with each other, both showing a dropping PDF tail below the H06 one at pIWP > 1000 g/m^2.

MLS 640-GHz $IWP_{>11km}$ overlaps with CloudSat in sensitivity over a narrow (5-100 g/m^2) range (Figure 9c). The R04 PDF at pIWP < ~5 g/m^2 starts to be questionable because it is dominated by noise and can be affected by truncated statistics in the R04 IWC retrieval. Although MLS $IWP_{>11km}$ shows a slightly better (0.8 g/m^2) precision than CloudSat, it becomes saturated at ~100 g/m^2. Compared to the PDF of ARM TWP $IWP_{>11km}$, CloudSat and MLS results exhibit a similar PDF slope but with a lower cloud occurrence frequency. Again, the different CloudSat retrievals agree well for small pIWPs but start to deviate from each other at pIWP > 1000 g/m^2.

In Figure 9(d), the CloudSat pIWP is compared with MODIS, AMSU-B, and ARM TWP observations. The CloudSat pIWP is integrated up from 3 km and we neglect clouds below that altitude where there is very little contribution. The estimated precision for CloudSat $IWP_{>3km}$ is ~9 g/m^2, and the three CloudSat retrievals show a consistent PDF up to ~ 5000 g/m^2. Between 10 and 5000 g/m^2, the ARM PDF agree relatively well with CloudSat except for a steeper slope at pIWP > 100 g/m^2. The ARM data are biased slightly high at small pIWPs and low at large pIWPs. As in MLS 115-GHz pIWP, the AMSU-B retrieval lacks sensitivity to mid- and high-latitude cloud ice (not shown). Both MODIS and AMSU-B pIWPs are biased high (by a factor of

5-8) at 10-1000 g/m^2 where the sensitivities are overlapped. The MODIS and AMSU-B PDFs drop sharply at IWP > 500 g/m^2 due to sensitivity loss with these techniques. It is interesting to observe that the passive IR and microwave techniques reveal a similar sensitivity loss at large pIWP values, which could be explained by their dependence on the vertical temperature gradient in the troposphere for cloud detection. It has been shown that the temperature gradient provide a similar dynamic range for IR and microwave cloud detections (Berg et al., 1999). As expected for the techniques with lower microwave frequencies, the AMSU-B retrieval (from 89-150 GHz) would have a similar PDF dropoff to the MLS 115 and 240 GHz retrievals. The large CloudSat-AMSU-B bias is unlikely caused by different spatial averagings between the two. The averaging difference between CloudSat (1.1 km by 1.8 km) and AMUS-B footprints (15 km diameter) would lower the CloudSat PDF by ~10%, which would worsen the CloudSat-AMSU-B bias. Thus, to reconcile the observed differences, one must re-examine the assumptions made on cloud microphysics in these retrievals.

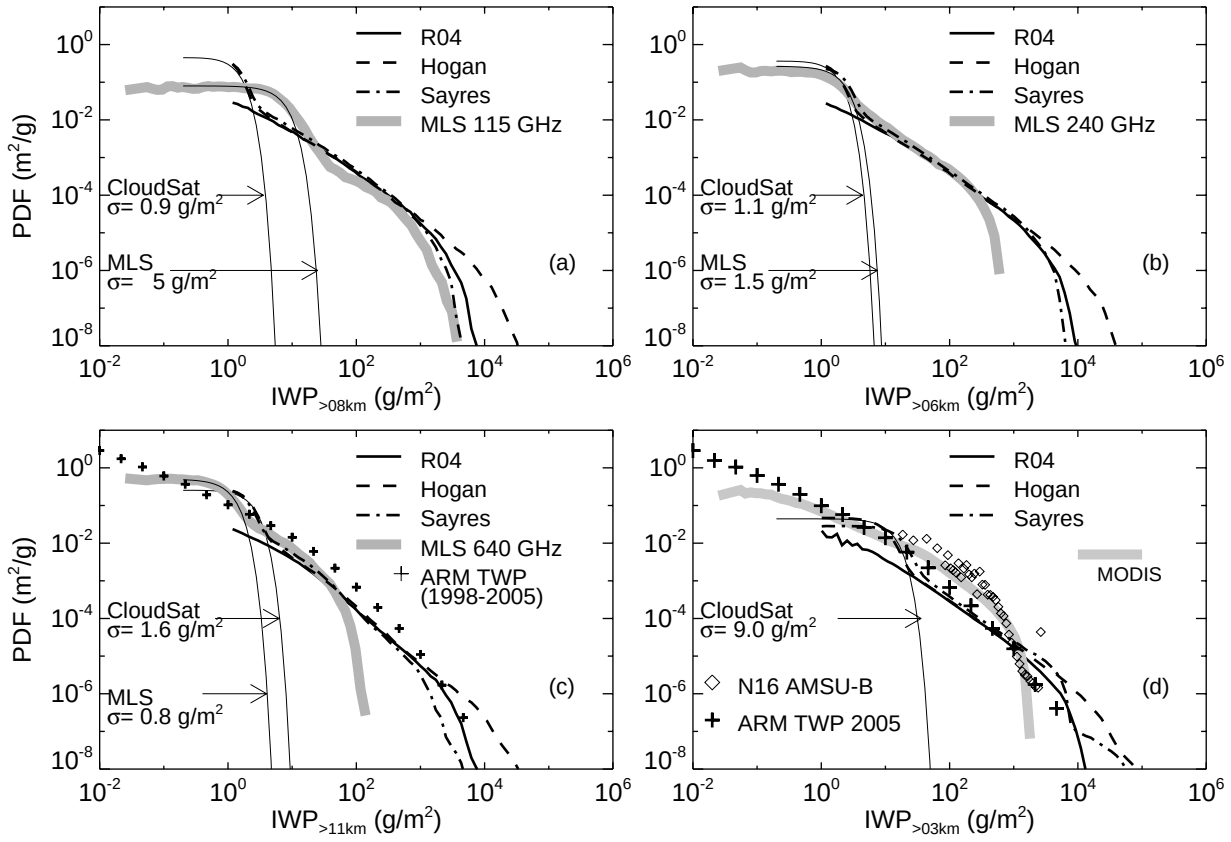

Figure 9. (a)-(c) PDFs of the tropical (25°S-25°N) IWPs from CloudSat R04, H06, S08, and MLS for 7 July-16 August 2006. The three partial IWPs correspond to MLS measurements from three different frequencies. To match CloudSat IWP to MLS measurement volume, we also average the CloudSat data horizontally with a running window of approximately 124, 61 and 29 km for comparison with MLS 115, 240 and 640 GHz observations, respectively. The rising PDF at small IWP values are fitted with a Gaussian function with σ=5, 0.8, and 1.5 g/m^2 for CloudSat, and σ=52, 4.2, and 0.1 g/m^2 for MLS. (*d*) PDFs of AMSU-B, ARM TWP, and CloudSat IWPs. Except for AMSU-B, all IWPs in this panel are a partial column above 3 km, or $IWP_{>3km}$. No spatial averaging is applied to CloudSat data, and a Gaussian function with σ=9 g/m^2 is fitted to the CloudSat H06 retrieval. The PDF of ARM TWP $IWP_{>3km}$ from 1998-2005 is also included in (*c*), and all the ARM data are from 3-h averaged measurements.

6 Conclusions and Future Work

We have compared statistical properties and global morphology of IWC and pIWP measurements from Aura MLS, CloudSat, and correlative data sets. Measurement noise, bias and sensitivity range of these data sets are characterized using the normalized PDF. The typical MLS IWC precision value increases with pressure, varying between 0.06 and 1 mg/m^3 at 83 and 215 hPa with sensitivity saturated at ~100 mg/m^3. The MLS pIWPs derived from 115, 240 and 640

GHz diagnosis T_{cir} represent a partial column with the bottom height of approximately 8, 6, and 11 km. The typical precision for these pIWPs are 5, 1.5, and 0.8 g/m^2 with sensitivity saturated at about 2000, 500, and 100 g/m^2, respectively.

Statistical properties of CloudSat reflectivity have also been studied in terms of the normalized PDF, and the estimated precision of cloud reflectivity is -31 dBZ, or ~3 dBZ better than the design requirement. In this study we compared three CloudSat IWC retrievals: R04 2B-IWC-RO, Hogan et al. (2006, or H06), and Sayres et al. (2008, or S08). In the upper troposphere (> ~8 km), all the retrievals show similar PDF distributions at IWC < 1000 mg/m^3, and the agreement between R04 and S08 extends to ~2000 mg/m^3. At the large IWCs, the R04 and S08 retrievals are significantly lower than H06. For IWC < ~500 mg/m^3, the three CloudSat retrievals have a PDF slope generally consistent with in-situ observations (particularly good agreement with CRYSTAL-FACE). The estimated precision of CloudSat IWC measurements varies from 0.4 mg/m^3 at 8 km to 1.6 mg/m^3 at 12 km. The R04 IWC is significantly improved over R03 in retrieving the large-IWC cases. However, the R04 IWC retrieval is quite larger than R03. The high bias is also reflected in CloudSat pIWPs derived from the retrieved IWC profile. The estimated precision for $IWP_{>3km}$ is ~9 g/m^2.

We compared MLS and CloudSat cloud ice measurements with other correlative data, and the main findings from this study are summarized as follows:

1) MLS V2.2 and CloudSat R04 retrievals show consistent IWC morphologies but the R04 mean is generally higher by a factor of ~5. Much of the high bias is due to MLS sensitivity degradation at large IWC values. The IWC PDFs agree reasonably well, showing biases less than 50% in the overlapped sensitivity range. At 15-17 km the R04 biases are high against MLS and increase rapidly with IWC. At these altitude, MLS IWC

has its best precision and usually is not limited by sensitivity degradation. Comparisons between MLS and R03 (Wu et al., 2008), on the other hand, show rather small biases. These MLS-CloudSat differences warrant a further investigation.

2) ECMWF monthly mean IWCs are lower compared to MLS V2.2 and CloudSat R04 retrievals by a factor of ~5 and ~20, respectively. The biases between ECMWF and the observations are IWC-dependent, showing that ECMWF is high at small IWCs but low at large IWCs. The PDF of ECMWF IWC drops off too rapidly at the large values. The differences between modeled and observed IWC must be interpreted with caution because cloud and precipitation ice are treated differently in the model whereas observing techniques usually cannot distinguish between the two. Similar model-observation differences are found in the PDF comparisons of GEOS-5.1, MLS and CloudSat IWCs.

3) The pIWPs from MLS 115, 240 and 640 GHz T_{cir} produce consistent monthly morphologies with those derived from CloudSat IWC. Lack of mid- and high-latitude cloud ice in MLS 115-GHz pIWP map is likely due to poor MLS sensitivity at this frequency, but lack of mid-latitude clouds in the 640-GHz pIWP map is mostly caused by MLS inability of penetrating into the mid-troposphere at 640 GHz. Compared to CloudSat, MLS 115-GHz pIWP is slightly high at large values but low at small values whereas MLS 640-GHz pIWP has a low bias by a factor of 2-3. The 240-GHz pIWP retrieval has the best agreement with CloudSat, showing a slightly low bias at small IWP values. All ECMWF pIWPs have a low bias compared to the observations, consistent with the low bias found in the IWC comparisons.

4) The AMSU-B and MODIS pIWPs show ~5× and ~8× high biases, respectively, against CloudSat for the values between 10 and 500 g/m^2. The high biases are most likely due to

assumptions made in these retrievals on cloud microphysics. Both AMSU-B and MODIS sensitivities start to decay at pIWP > 500 g/m^2 due to saturation.

We have learned from this study that the dynamic range of cloud ice variability is so large that no single instrument can measure all. Individual techniques are often limited by measurement noise at small IWC values and sensitivity degradation at large values. With the launch of CloudSat and CALIPSO, cloud remote sensing has entered into a new era. These active sensors greatly extend the cloud sensitivities from passive sensor like MLS, AMSU-B and MODIS instruments, but the passive sensors will likely remain as the key technique in the future to provide 2D or 3D coverage. Joint analyses of the A-Train active-passive cloud data have an important implication for future cloud remote sensing, particularly in reducing cloud ice uncertainties associated with cloud microphysics. For example, intercomparisons of radiative transfer modeling for collocated cloud measurements will lead to additional constraints on the cloud microphysics assumptions used in the retrievals. To better understand cloud and precipitation ice, the 13.8-GHz TRMM PR (Tropical Rainfall Measuring Mission Precipitation Radar) data (1998-present) has an extended sensitivity to precipitation ice that can be used to further constrain microphysical properties. Together, these instruments now provide sensitivity needed to cover the entire dynamic range of cloud and precipitation ice, and the satellite observations begin to show appreciable precision and accuracy for climate models to probe the cloud feedback problem in the Earth's climate system.

Acknowledgments

This work was performed at the Jet Propulsion Laboratory, California Institute of Technology, under contract with the National Aeronautics and Space Administration (NASA). We thank our MLS and CloudSat colleagues for successful instrument operation and data

processing. For this study, we specially thank Drs. Gerald Mace, Robin Hogan and Alain Protat for valuable discussions on radar algorithms. We also thank ECMWF for providing their analyses data to JPL and the AIRS team for helping to access the data. Efforts in CIRA (Cooperative Institute for Research in the Atmosphere) for making AMSU-B data available are also acknowledged.

References

Acarreta, J. R., J. F. de Haan, and P. Stammes, Cloud pressure retrieval using the O2-O2 absorption band at 477 nm, *J. Geophys. Res*., **109**, D05204, doi:10.1029/2003JD003915, 2004.

Atlas, D., S. Y. Matrosov, A. J. Heymsfield, M.-D. Chou, and D. B. Wolf, Radar and radiation properties of ice clouds, *Journal of Applied Meteorology*, *34*, 2329–2345, (995.

Austin, R. T., and G. L. Stephens, Retrieval of stratus cloud microphysical parameters using millimeter-wave radar and visible optical depth in preparation for CloudSat. 1. Algorithm formulation. *J. Geophys. Res*., **106**, 28,233-28,242, 2001.

Austin, R. T., A. J. Heymsfield, and G. L. Stephens, Retrievals of ice cloud microphysical parameters using the CloudSat millimeter-wave radar and temperature, submitted to *J. Geophys. Res*., CloudSat special section, 2008.

Aydin, K., and C. X. Tang, Relationships between IWC and polarimetric radar measurands at 94 and 220 ghz for hexagonal columns and plates, *Journal Of Atmospheric And Oceanic Technology*, *14*, 1055–1063, 1997.

Barnes, W. L., T. S. Pagano, and V. V. Salomonson, Prelaunch characteristics of the Moderate Resolution Imaging Spectroradiometer (MODIS) on EOS-AM1. *IEEE Trans. Geosci. Remote Sens.,* **36,** 1088–1100, 1998.

Bauer, P., G. Kelly, and E. Andersson, SSM/I radiance assimilation at ECMWF. Proc ECMWF/GEWEX workshop on "Humidity Analysis", Reading, 8-11 July 2002, 167-175, 2002.

Benedetti, A., G. L. Stephens, J. M. Haynes, Ice cloud microphysics retrievals from millimeter radar and visible optical depth using an estimation theory approach. *J. Geophys. Res.*, **108**, D11, 4335, doi:10.1029/2002JD002693, 2003.

Berg, W., J. J. Bates, and D. L. Jackson, Analysis of upper-tropospheric water vapor brightness temperatures from SSM/T2, HIRS, and GMS-5 VISSR, *J. Appl. Meteor.*, **38**, 580-595, 1999.

Bloom, S. C., et al., The Goddard Earth Observing Data Assimilation System, GEOS DAS Version 4.0.3: Documentation and validation, *Tech. Rep. 104606 V26*, NASA, 2005.

Brown, P. R. A., et al., The role of spaceborne millimeter-wave radar in the global monitoring of ice cloud, *Journal of Applied Meteorology*, *34*, 2346–2366,1995.

Chevallier F., P. Lopez, A. M. Tompkins, M. Janisková, and E. Moreau The capability of 4D-Var systems to assimilate cloud-affected satellite infrared radiances, *Quart. J. Roy. Meteor. Soc.*, **130**, 917-932, 2004.

Clothiaux, E. E, et al.. Objective Determination of Cloud Heights and Radar Reflectivities Using

a Combination of Active Remote Sensors at the ARM CART Sites. *Journal of Applied Meteorology* 39: 645-665, 2000.

Clothiaux, E.E., et al., The ARM Millimeter Wave Cloud Radars (MMCRs) and the Active Remote Sensing of Clouds (ARSCL) Value Added Product (VAP), DOE Tech. Memo. ARM VAP-002.1, U.S. Department of Energy, Washington, D.C., 2001.

Deng, M., and G. G. Mace, Cirrus microphysical properties and air motion statistics using cloud radar Doppler moments. Part I: Algorithm description. *J. Appl. Meteor.*, **45** (12): 1690-1709, 2006.

Eriksson, P., Ekstrom, M., Rydberg, B., and Murtagh, D. P., First Odin sub-mm retrievals in the tropical upper troposphere: ice cloud properties, *Atmos. Chem. Phys*., **7**, 471–483, 2007.

Eriksson, P., et al., Comparison between first Odin-SMR, Aura MLS and CloudSat retrievals of cloud ice masses in the upper tropical troposphere, *Atmos. Chem. Phys. Diss*., in review, 2008.

Evans, K. F., et al., Modeling of submillimeter passive remote sensing of cirrus clouds. *J. Appl. Meteor.*, **37**, 184-205, 1998.

Gill, A. E., Some simple solutions for heat-induced tropical circulation. *Quart. J. Roy. Meteor. Soc*., **106,** 447–662, 1980.

Halpern, D, and C. W. Hung, Satellite observations of the southeast Pacific intertropical convergence zone during 1993-1998. *J. Geophys. Res.*, **106**, 28107–28112, 2001.

Hartmann, D. L., and K. Larson, An important constraint on tropical cloud - climate feedback, *Geophys. Res. Lett*., **29** (20): doi:10.1029/2002GL015835, 2002

Heymsfield, A. J., and C. M. R. Platt, A parameterization of the particle size spectrum of ice clouds in terms of the ambient temperature and the ice water content. *J. Atmos. Sci*., **41**, 864-855, 1984.

Heymsfield, A. J., and G. M. McFarquhar, 1996: On the high albedos of anvil cirrus in the tropical Pacific warm pool: Microphysical interpretations from CEPEX. *J. Atmos. Sci.,* **53,** 2424–2451.

Heymsfield, A. J., A. Bansemer, P. R. Field, S. L. Durden, J. L. Stith, J. E. Dye, W. Hall, and C. A. Grainger: Observations and parameterizations of particle size distributions in deep tropical cirrus and stratiform precipitating clouds: Results from in situ observations in TRMM field campaigns. *J. Atmos. Sci*., **59**, 3457-3491, 2002.

Heymsfield, A. J., A. Bansemer, C. Schmitt, C. Twohy and M. R. Poellot. Effective Ice Particle Densities Derived from Aircraft Data. *J. Atmos. Sci.*, **61**, 982–1003, 2004.

Heymsfield, A. J., Z. Wang, and S. Matrosov, Improved radar ice water content retrieval algorithms using coincident microphysical and radar measurements, *J. Appl. Meteorol*., **44**, 1391-1412, 2005.

Heymsfield, A. J., et al., Testing IWC retrieval methods using radar and ancillary measurements with in-situ data. *J. Appl. Met. Clim.*, in press. 2007.

Hogan, R. J., et al., Characteristics of mixed-phase clouds. I: Lidar, radar and aircraft observations from CLARE'98, Q. J. Royal Meteor. Soc., **129** (592): 2089-2116 Part A 2003.

Hogan, R. J., M. P. Mittermaier, and A. J. Illingworth, The retrieval of ice water content from radar reflectivity factor and temperature and its use in evaluating a mesoscale model. *J.Appl. Meteor.*, 45, 301-317, 2006.

Hong, G., G. Heygster, J. Miao, and K. Kunzi, Detection of tropical deep convective clouds from AMSU-B water vapor channels measurements. *J. Geophys. Res*., **110**, D05205, doi:10.1029/2004JD004949, 2005.

Houghton, J. T., Y. Ding and M. Noguer, Climate Change 2001: The scientific basis, Cambridge University Press, 881 pp. 2001.

Houze, Jr., R. A., S. S. Chen, D. E. Kingsmill, Y. Serra, and S. E. Yuter, Convection over the Pacific Warm Pool in relation to the atmospheric Kelvin-Rossby wave. *J. Atmos. Sci*., **57**, 3058-3089, 2000.

Im, E., S. L. Durden, and C. Wu, "Cloud Profiling Radar for the CloudSat mission," *IEEE Aerosp. Electron. Syst. Mag.*, vol. 20, pp. 15-18, October 2005.

Intrieri, J. M., G. L. Stephens, W. L. Eberhard, and T. Uttal, A Method for Determining Cirrus Cloud Particle Sizes Using Lidar and Radar Backscatter Technique*, J. Appl., Meteor.,* **36**, No. 6, pp1074-1082, 1993.

Jarnot, R.F., V.S. Perun, and M.J. Schwartz, Radiometric and spectral performance and calibration of the GHz bands of EOS MLS, *IEEE Trans. Geosci. Remote Sensing 44,* no. **5**, 1131-1143, May 2006.

Li, J.-L., et al., Comparisons of EOS MLS Cloud Ice Measurements with ECMWF analyses and GCM Simulations: Initial Results, *Geosphys. Res. Lett.* **32** , L18710, doi:10.1029/2005GL023788, 2005.

Li, J.-L., J.H. Jiang, D.E. Waliser, and A.M. Tompkins, Assessing Consistency between EOS MLS and ECMWF Analyzed and Forecast Estimates of Cloud Ice, *Geophys. Res. Lett.*, in review. 2007.

Li, L., and S. L. Durden, Level 1 B CPR Process Description and Interface Control Document, JPL Document No. D-20308, 2006.

Li, Q. B., et al., Convective outflow of South Asian pollution: A global CTM simulation compared with EOS MLS observations, *Geophys. Res. Lett. 32*, no. **14**, L14826, doi:10.1029/2005GL022762, 2005.

Lietzke, Christopher E., Clara Deser, and Thomas H. Vonder Haar, 2001: Evolutionary structure of the eastern Pacific double ITCZ based on satellite moisture profile retrievals. J. Climate, 14, 743–751.

Liu, C., and A. J. Illingworth, Toward more accurate retrievals of ice water content from radar measurements of clouds, J. Appl. Meteorol., 39, 1130–1146, 2000.

Liu, G., and J. A. Curry, Topical ice water amount and its relations to other atmospheric hydrological parameters as inferred from satellite data. *J. Appl. Meteor.*, **38**, 1182-1194, 1999.

Liu, W. T., and X. Xie, Double intertropical convergence zones—A new look using scatterometer. *Geophys. Res. Lett.,* **29,** 2072, doi:10.1029/2002GL015431, 2002.

Mace, G. G., E. E. Clouthiaux, and T. P. Ackerman, The composite characteristics of cirrus clouds: Bulk properties revealed by one year of continuous cloud radar data. *J. Climate*, **14**, 2185-2203, 2001.

Mace, G. G., R. Marchand and G. L. Stephens, Global Hydrometeor Occurrence as Observed by CloudSat; Initial Observations from Summer 2006, *Geophys. Res. Lett.,* Vol. 34, L09808, doi:10.1029/2006GL029017, 2007.

Matrosov, S. Y., A. V. Korolev, and A. J. Heymsfield, Profiling cloud mass and particle characteristic size from Doppler radar measurements, J. *Atmos. Oceanic Technol*., 19, 1003–1018, 2002.

McFarquhar, G. M., and A. J. Heymsfield, Microphysical characteristics of three anvils sampled during the central equatorial pacific experiment. *J. Atmos. Sci*., **53**, 2401-2423, 1996.

McFarquhar, G. M., and A. J. Heymsfield, Parameterization of tropical cirrus ice crystal size

distributions and implications for radiative transfer: Results from CEPEX. *J. Atmos. Sci.*, **54**, 2187-2200, 1997.

Protat, A., J. Delanoe, and D. Bouniol, A. J. Heymsfield, A. Bansemer, and P. Brown, Evaluation of ice water content retrievals from cloud radar reflectivity and temperature using a large airborne in-situ microphysical database. *J. Appl. Meteor. Clim.*, **46**, 557-572, 2007.

Ramanathan, V., R. D. Cess, E. F. Harrison, et al., Cloud-radiative forcing and climate - results from the Earth radiation budget experiment. *Science* **243**, 57-63, 1989.

Randall et al., Climate models and their evaluation, *Climate Change 2007: The Physical Sciences Basis*, Chap.8, 2007.

Sassen, K., Ice cloud content from radar reflectivity. *J. Climate* Appl. Meteor., **26,** 1050–1053, 1987.

Sassen, K., Z. Wang, V. I. Khvorostyanov, G. L. Stephens, and A. Bennedetti, Cirrus cloud ice water content radar algorithm evaluation using an explicit cloud microphysical model. *J. Appl. Meteor.,* **41,** 620–628, 2002.

Sayres, D. S., J. B. Smith, J. V. Pittman, E. M. Weinstock, J. G. Anderson, G. Heymsfield, L. Li, A. M. Fridlind, A. S. Ackerman, Validation and determination of ice water content radar reflectivity relationships during CRYSTAL-FACE: Flight requirements for future comparisons. Submitted to *J. Geophys. Res.*, 2008.

Salomonson, V.V., W. L. Barnes, P.W. Maymon, H. E. Montgomery, H. Ostrow, MODIS: advanced facility instrument for studies of the Earth as a system, *IEEE Trans. Geosci. Remote Sensing,* **27**, 145 – 153, 1989.

Stephens, G. L., Radiation profiles in extended water clouds, II, Parameterizations schemes, *J. Atmos. Sci.*, **35**, 2123-2132, 1978.

Stephens, G. L., Cloud feedbacks in the climate system: A critical review, *J. Climate*, **18**, 237-273, 2005.

Stephens, G. L., et al., The CloudSat mission and the EOS constellation: A new dimension of space-based observations of clouds and precipitation. *Bull. Amer. Meteor. Soc.,* **83,** 1771–1790, 2002.

Stephens, G. L., and C. D. Kummerow, The remote sensing of clouds and precipitation from space: A review. *J. Atmos. Sci.*, **64**, 3742-3765, 2007.

Tanelli, S., et al., CloudSat's Cloud Profiling Radar after 1 year in orbit: performance, external calibration, and processing*, IEEE Trans. Geos. Rem. Sens.*, submitted, 2008.

Waliser, D. E., and C. Gautier, A satellite-derived climatology of the ITCZ, *J. Climate*, **6**, 2162-2174, 1993.

Waliser, D. E., et al., ????, JGR, CloudSat special section, 2008.

Waters, J.W., et al., The Earth Observing System Microwave Limb Sounder (EOS MLS) on the Aura satellite, *IEEE Trans. Geosci. Remote Sensing 44,* no. **5**, 1075-1092, May 2006.

Weng, F., and N. C. Grody, Retrieval of ice cloud parameters using a microwave imaging radiometer. *J. Atmos. Sci.*, **57**, 1069-1081, 2000.

Wu, D. L., W. G. Read, A. E. Dessler, S. C. Sherwood, and J. H. Jiang, UARS MLS Cloud Ice Measurements and Implications for H_2O Transport near the Tropopause, *J. Atmos. Sci*., **62** (2): 518-530, 2005.

Wu, D.L., J.H. Jiang, and C.P. Davis, EOS MLS cloud ice measurements and cloudy-sky radiative transfer model, *IEEE Trans. Geosci. Remote Sensing 44,* no. **5**, 1156-1165, May 2006.

Wu, D. L., et al., Validation of Aura Microwave Limb Sounder (MLS) IWC measurement, *J.*

Geophys. Res., Aura special section, in press, 2008.
Zhao, L., and F. Weng (2002), Retrieval of ice cloud parameters using the Advanced Microwave Sounding Unit, J. Appl. Meteorol., 41, 384– 395.

Appendices

A. Normalized Probability Density Function (PDF)

The PDF analysis provides great insights to statistical properties of a data set and can be used to compare these properties among different data sets without imposing strict collocation-and-coincidence requirements. Particularly for cloud comparisons, the collocation-and-coincidence requirements are sometimes too difficult to meet, which leave with too few samples to draw any conclusion. The PDF should be normalized such that the area under the distribution is unity. Comparing cloud observations in form of normalized PDF require no cloud detection threshold, which can be problematic in the case where sensors have different sensitivities. Cloud occurrence frequency and fraction are among the quantities of this kind, and they are highly sensor-dependent or even platform-dependent. As shown in Fig A-1, the normalized PDF preserves many important statistical properties of a data set, from which one determine measurement noise, bias, and sensitivity, collectively.

If the statistics of a data set are full preserve (i.e., no artificial truncation imposed), the measurement noise will show up as a Gaussian function in small values. In a log-log coordinate, the noise manifest itself as a rising curve in the normalized PDF. Usually, the noise PDF is symmetric about zero, which can be verified with the PDF of negative IWC or IWP values. In other words, if a measurement is not significantly above its noise, it should be categorized as a clear sky. Thus, a threshold for defining clear vs cloudy skies will induce the cases like false alarm and missing clouds (Fig A-1). In a comparison between two data sets, a bias or scaling error would appear as distorted or shifted PDFs relative to each other. Degradation in sensitivity due to saturation to large IWC or IWP cases would result in a sharp dropoff in PDF drop at those values.

One of the disadvantages with the PDF method is the lack of information on spatial distribution. In other words, one can swap cloud statistics between regions A and B, and make no difference in the final PDF statistics. In this concern the PDF analysis may be less useful for very nonlinear retrieval systems where the resulting PDFs have little dependence on changes in the method.

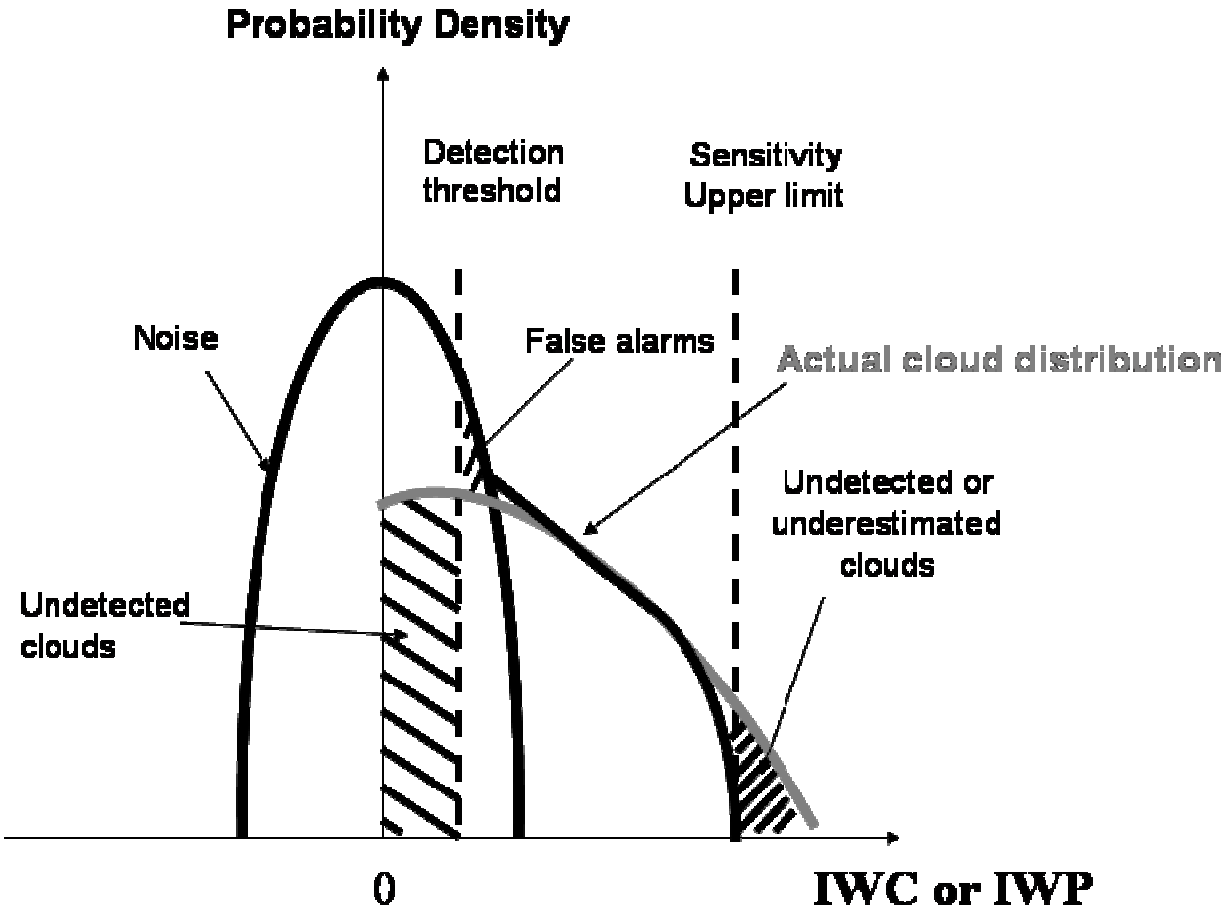

Fig A-1 A schematic diagram to illustrate different portions of a measured cloud PDF. The grey curve is the true PDF from a cloud ice ensemble that is only measured partially by a sensor (solid black) due to measurement noise and sensitivity limitation. Depending on the threshold used for cloud detection, false cloud detection and missing clouds are unavoidable and can become a problem to compare cloud occurrence frequency from different sensors. Directly comparing the normalized PDFs from different sensors can identify measurement noise, sensitivity range and accuracy in a cloud ice data set.